TriDurLE

National Center for Transportation Infrastructure Durability & Life-Extension

Project ID: 2022-FAU-02

Inversion of poro-elastic sound propagation model and measurement to monitor both rebar corrosion and crack formation using high frequency ultrasonics and contact transducers.

Final Report

By

Pierre-Philippe Beaujean, PhD

for

National University Transportation Center TriDurLE
Department of Civil & Environmental Engineering
405 Spokane Street PO Box 642910
Washington State University Pullman, WA 99164-2910

7/29/2024

Acknowledgements

The author is indebted to the USDOT and TriDurLE for financial support and FAU for matching support. The author also acknowledges the assistance of his colleague Dr. Francisco Presuel-Moreno (Marine Materials and Corrosion Laboratory), and two students who worked as graduate research assistants during the duration of this project: Matthew Cole Brogden (Acoustics Laboratory) and Samuel Shaffer (Acoustics Laboratory).

Disclaimer

Table of Contents

Contents

List of Figures

List of Tables

Executive Summary

The detection and measurement of rebar corrosion in reinforced concrete using ultrasonic Non-Destructive Testing (NDT) has been of great interest for several decades, as the operator can monitor corrosion in reinforce concrete and ideally detect early signs of corrosion, without any need to drill through or cut the concrete. The limitation of this approach resides in the ability to successfully detect early forms of corrosion before cracks reach the surface of the reinforced concrete.

The goal is to demonstrate the ability to detect early appearance of cracks in reinforced concrete due to rebar corrosion, using ultrasonic nondestructive acoustic testing with no direct contact between the sensor and the concrete block, in conjunction with a poro-elastic ultrasound propagation model.

The objectives are threefold: (1) Identify the proper measurement configuration and predict the performance, using the modeling of the ultrasound propagation in the reinforced concrete; (2) Perform a series of targeted measurements using the proper ultrasonic transducers on a set of existing reinforced concrete samples placed in partial or complete immersion; (3) Evaluate the degree of corrosion within the reinforced concrete with confidence levels according to the poro-elastic model, and correlate the results with those obtained (separately from this proposal) using traditional non-invasive techniques (e.g. corrosion current and corrosion potential measurements).

The proposed poro-elastic model ties the physical properties of the porous medium (such as porosity, mean grain diameter, mass density, bulk modulus, shear modulus) to the sound propagation through the porous medium. It can also handle gradual changes of the physical characteristics of the medium and produce a synthetic response to a broadband acoustic impulse. This technique is very relevant in the material observed around the corroding bar.

Chapter 1. Introduction

1.1 Problem Statement

The detection and measurement of rebar corrosion in reinforced concrete using ultrasonic Non-Destructive Testing (NDT) has been of great interest for several decades, as the operator can monitor corrosion in reinforce concrete and ideally detect early signs of corrosion, without any need to drill through or cut the concrete. The limitation of this approach resides in the ability to successfully detect early forms of corrosion before cracks reach the surface of the reinforced concrete.

This research would be the foundation for a more detailed acoustic analysis of rebar corrosion detection in reinforced concrete pilings/columns out in the field.

1.2 Objectives

The goal is to demonstrate the ability to detect early appearance of cracks in reinforced concrete due to rebar corrosion, using ultrasonic nondestructive acoustic testing with no direct contact between the sensor and the concrete block, in conjunction with a poro-elastic ultrasound propagation model.

The objectives are threefold: (1) Identify the proper measurement configuration and predict the performance, using the modeling of the ultrasound propagation in the reinforced concrete; (2) Perform a series of targeted measurements using the proper ultrasonic transducers on a set of existing reinforced concrete samples placed in partial or complete immersion; (3) Evaluate the degree of corrosion within the reinforced concrete with confidence levels according to the poro-elastic model, and correlate the results with those obtained (separately from this proposal) using traditional non-invasive techniques (e.g. corrosion current and corrosion potential measurements).

The proposed poro-elastic model ties the physical properties of the porous medium (such as porosity, mean grain diameter, mass density, bulk modulus, shear modulus) to the sound propagation through the porous medium. It can also handle gradual changes of the physical characteristics of the medium and produce a synthetic response to a broadband acoustic impulse. This technique is very relevant in the material observed around the corroding bar.

1.3 Expected Contributions

At this stage of the project, the contributions are as follow: (i) The development and testing of the poro-elastic model for the reinforced concrete samples has been completed; (ii) Ultrasonic data and rebar potential data have been collected on a limited number of reinforced concrete samples; (iii) Processing of simulated data sets and comparison between simulated and measured data were completed; (iv) A non-linear solver using Trust-Region Reflective (TRR) algorithm has been developed, to optimize the coefficient matching between model and experimental data.

In the longer term, using the proposed approach, the detection of pre-cracking corrosion and early-stage post-cracking corrosion becomes possible.

Pre-cracking corrosion would translate into two phenomena: (i) A change in the characteristic impedance of the rebar in contact with the concrete, causing predominantly a change in the amplitude of the rebar

echo; (ii) A change in the diameter of the rebar, which would produce a change in the time-of-travel difference between surface echo and rebar echo.
Post-cracking corrosion would translate into two phenomena: (i) An accentuated change in the characteristic impedance of the rebar in contact with the concrete (in comparison with the pre-cracking corrosion case), causing predominantly an accentuated change in the amplitude of the rebar echo; (ii) The appearance of an additional echo due to the presence of forming cracks.

Differentiating in time between the crack echo and rebar echo would be difficult due to their proximity. However, post-cracking corrosion will result in a very different signature from pre-cracking corrosion, which in turn will generate significantly different matching parameters in the poro-elastic model. For this reason, post-cracking corrosion is very likely to be detected and identified.

1.4 Report Overview

A literature review is provided in Chapter 2. The methodology is presented in Chapter 3. This chapter comprises an overview of the proposed approach, a description of the poro-elastic acoustic model and associated physical parameters of the reinforced concrete, and a description of the nonlinear solver used to improve the accuracy of the physical parameters. Chapter 4 covers the results and discussion. This chapter includes a description of the initial concrete sample modeling and experimentation. It also includes a description of the ongoing experimentation and analysis of a new set of concrete samples. Chapter 5 contains the summary and conclusions and is followed with a list of cited references.

Chapter 2. Literature Review

The detection and measurement of rebar corrosion in reinforced concrete using ultrasonic Non-Destructive Testing (NDT) has been of great interest for several decades. The benefit is obvious: using ultrasonic NDT, the operator can monitor corrosion in reinforce concrete and ideally detect early signs of corrosion, without any need to drill through or cut the concrete. The limitation of this approach resides in the ability to successfully detect early forms of corrosion, before cracks reach the surface of the reinforced concrete. Recent publications indicate that the scientific community is testing a variety of signal processing approaches to accurately estimate the propagation of cracks and changes in the rebar diameter, using narrow-beam, broadband acoustic transducers. Such transducers are operated at hundreds of [kHz], with [mm] scale resolution. These approaches include higher-order statistics, Short-Time Fourier Transform analysis (STFT), Artificial Neural-Networks (ANN) (Y. Xu et al., 2018), Convolutional Neural Network (CNN) (An et al., 2018), Wavelet Decomposition (WD) (Chang et a., 2019), Empirical Mode Decomposition (EMD) (Lin et al., 2009) among others (J. Xu et al., 2019). Such state-of-the-art techniques have great merit, but are limited in several ways:

- The techniques presented rely one way or another on distance measurement, obtained from the time-of-travel of sound and an estimate of the sound speed in the concrete and rebar. Propagation of ultrasounds through concrete is subject to great attenuation, mostly due to friction and scattering (Prassianakis et al., 2004). Such attenuation increases significantly with frequency, while spatial resolution improves as the frequency of operation (thus the effective frequency bandwidth of the transducer) increases (Philippidis et al., 2005). As a result, ultrasonic transducers used to monitor reinforced concrete are often operated around 500 [kHz], so that sound can travel through several [cm] of concrete, reach the rebar and produce a sufficiently strong echo, all of this with a resolution of the order of 5-to-15 [mm] (depending on the transducer bandwidth and actual speed of sound in the concrete) (Chaix et al., 2003; Laureti et al., 2018). One should note that many techniques exist (shear probes, contact transducers, focused and unfocused immersion transducers) and that the angle of observation can be adjusted (Panametrics, 2010). But it remains that the resolution is not sufficient to observe cracks a few [mm] long or less, which in turn limits the ability for an early detection.

- These techniques require either algorithm training (ANN, CNN), thorough observation of damaged samples, or an acoustic propagation model:
  - In the first case, the performance of the approach depends heavily on the number of training samples available and is limited to the statistical representativity of such samples. Considering the [mm] scale resolution of the transducers, the highly anisotropic nature of concrete and the strong variation in shape and composition of the corroded areas, such statistical representativity can only be achieved through very large number of concrete samples.
  - In the second case, the published approaches rely on simple acoustic models to translate the acoustic signal into actual estimates of the actual damaged occurring in the rebar and the concrete. Elastodynamic Finite Integration Technique (EFIT) (Fellinger et al., 1995), volume scattering models and similar Finite Element Analysis tools (COMSOL, ANSYS) are commonly used (Molero et al., 2014; Nakahata et al., 2015): while such techniques have great merit and produce results of great quality, they rely on a purely elastic model.

Sample observation clearly indicates that, in the vicinity of corrosion and crack, there is a complex structure combining fluid cavities and loose concrete material surrounding the corroded rebar (Presuel, 2015; Presuel et al., 2018). This means that a more appropriate acoustic propagation model is the poro-elastic model, such as the well-established Biot (Biot, 1956; Biot, 1962) and Biot-Stoll (Stoll, 1977) models developed for the propagation of sound in the seafloor. In both cases, fluid-filled cavities and a skeletal frame produce couple vibrations induced by the incoming sound, resulting in a dispersive medium where two types of compressional waves (the fast wave and the slow wave) and shear waves propagates. The frequency response of a poro-elastic medium is different from that of an elastic or even visco-elastic medium.

The Biot-Stoll model (derived from the original Biot model), although complex, has the great benefit of tying the physical properties of the porous medium (such as porosity, mean grain diameter, mass density, bulk moduli, shear moduli and so on) to the sound propagation through the porous medium. As such, it is possible to fit a set of physical characteristics of the medium to a specific acoustic signature measured off a transducer. While the Biot-Stoll model has been extensively used for foundation engineering and Navy purposes over the past fifty years, it has not been applied to the problem studied here. In addition, the Principal Investigator has studied and published a specific technique, derived from the initial work by Stern (Stern et al., 1985), to handle gradual changes of the physical characteristics of the medium and produce a synthetic response of such a porous medium to a broadband acoustic impulse (Beaujean, 1995; Beaujean et al., 2006; Joussein, Beaujean and Schock, 2004). To be clear, such a model can handle the propagation of sound through a pure fluid, a solid and a corroding porous medium. This technique is very relevant at the acoustic frequencies used and in material observed around the corroding bar.

Chapter 3. Methodology

3.1 Overview

The overall approach is depicted in Figures 1 and 2. The approach consists in analyzing a limited series of reinforced concrete samples provided by the Corrosion Laboratory (Florida Atlantic University, Department of Ocean and Mechanical Engineering, under the lead of Dr. Presuel-Moreno) using a narrow-beam high-frequency submerged transducer operated at 500 [kHz]. In this case, the author uses an Olympus Panametrics V389 (Panametrics, 2010) connected to an HP8112A high-frequency impulse generator and a Tektronix DPO3014, already available in the author's laboratory. This work was presented during a TriDurLE symposium in December 2021 (Beaujean et al., 2021; Brogden et al., 2021).
Regarding the detection ability in the field, two aspects must be considered: the transducer aspect and the signal processing aspect. It is understood that a submerged transducer is not necessarily the most practical choice in field operation. In the longer term, the author intends on testing the approach using a contact transducer. Using a contact transducer will not modify the proposed approach, which is entirely based on the acoustic signature of the signal as it travels through the concrete to the rebar.
Regarding the signal processing aspect, we must keep in mind that the Panametrics V389 immersion transducer is operated at 500 [kHz] with a pulse length of 7 [µs], which corresponds to a range resolution of nearly 16 [mm] (using an estimated 4500 [m/s] for the compressional sound speed in concrete), while the acoustic wavelength is 9 [mm]. This unfocused transducer also has a beamwidth of 14 [deg] at -6 [dB] in the concrete, which corresponds to an across-range resolution of 12 [mm].
Using this transducer, pre-cracking corrosion would translate into two phenomena:

- A change in the characteristic impedance of the rebar in contact with the concrete, causing predominantly a change in the amplitude of the rebar echo.
- A change in the diameter of the rebar, which would produce a change in the time-of-travel difference between surface echo and rebar echo.

Also, post-cracking corrosion would translate into two phenomena:

- An accentuated change in the characteristic impedance of the rebar in contact with the concrete (in comparison with the pre-cracking corrosion case), causing predominantly an accentuated change in the amplitude of the rebar echo.
- The appearance of an additional echo due to the presence of forming cracks. Differentiating in time between the crack echo and rebar echo would be difficult due to their proximity. However, post-cracking corrosion will result in a very different signature from pre-cracking corrosion, which in turn will generate significantly different matching parameters in the poro-elastic model. For this reason, post-cracking corrosion is very likely to be detected and identified.
- Detection and identification of pre-cracking corrosion is expected to be more challenging than that of post-cracking corrosion.

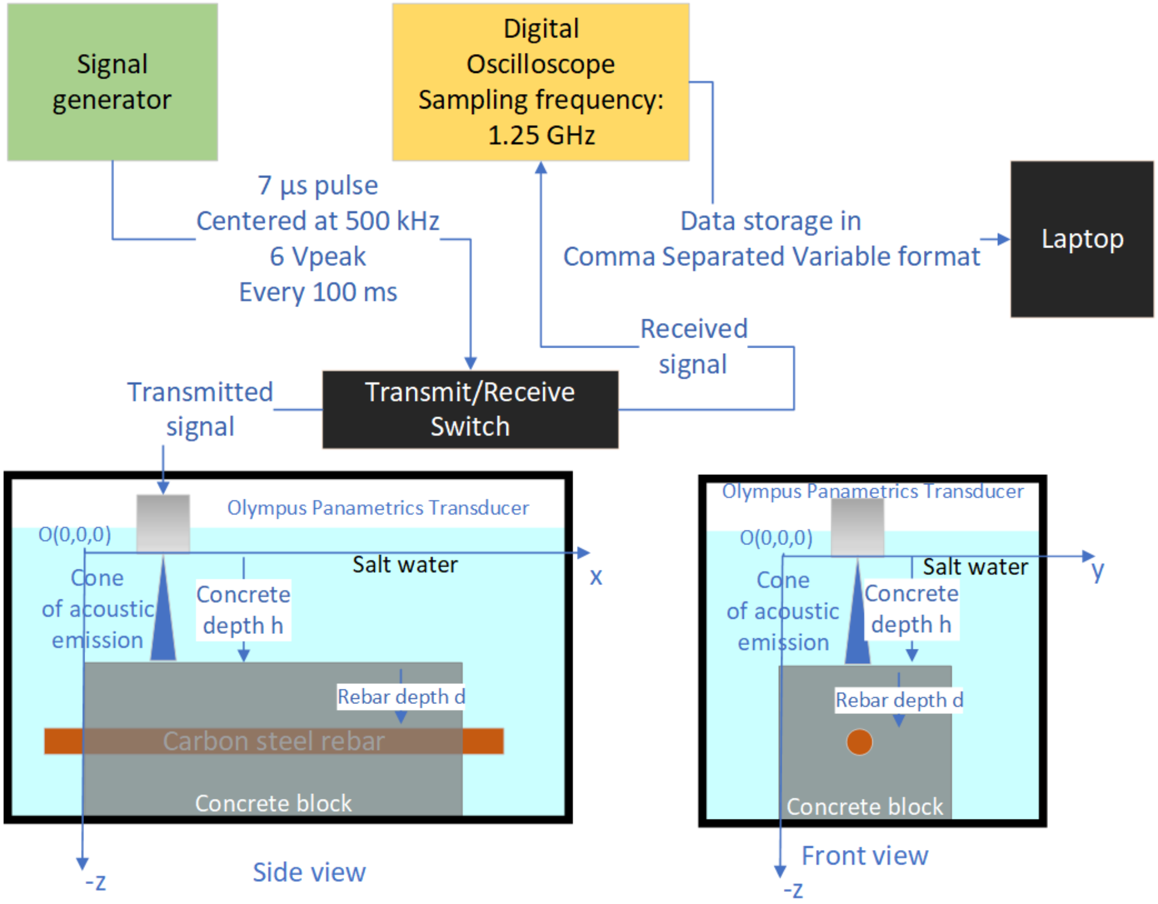

Figure 1. Experimental setup.

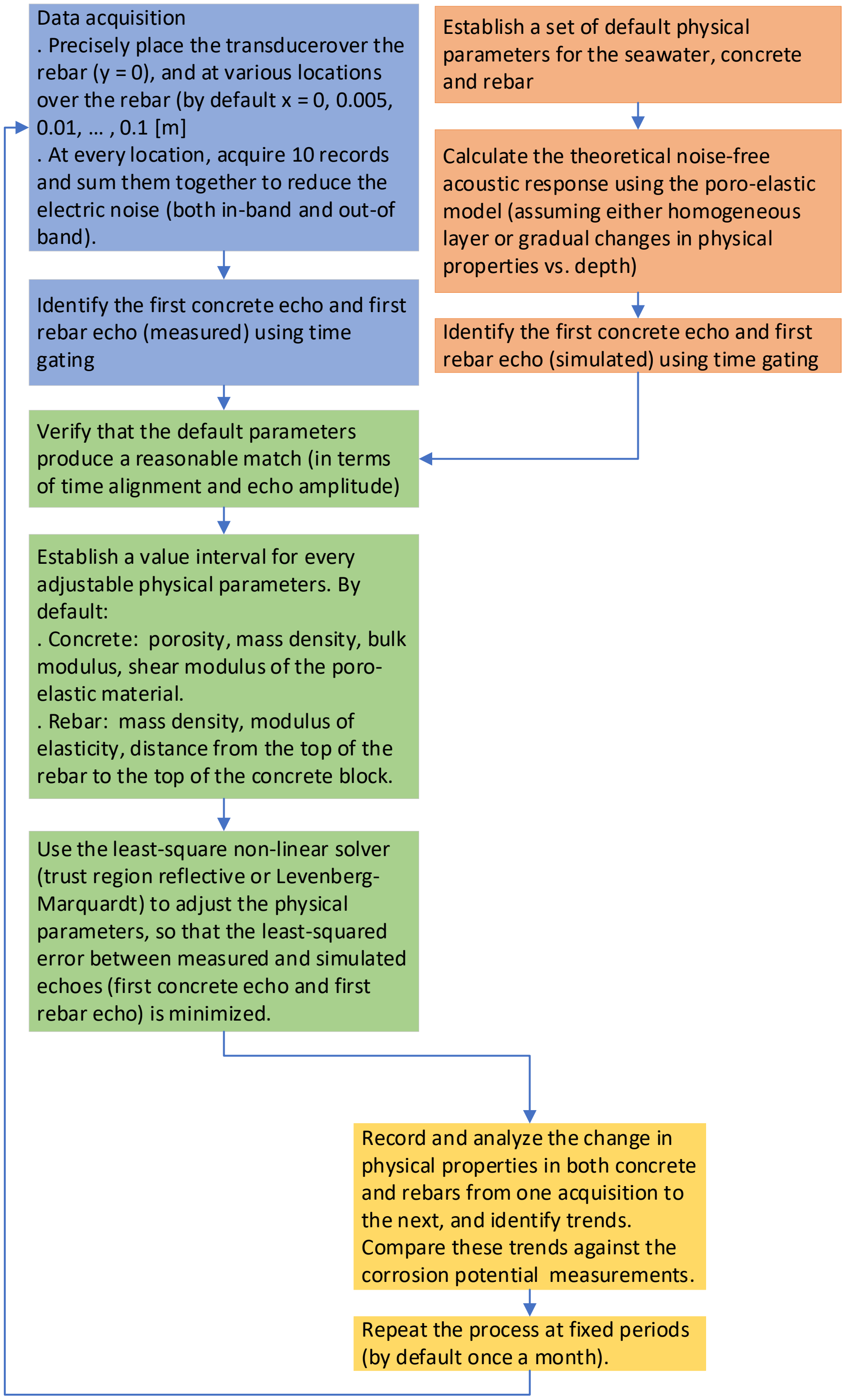

Figure 2. Process for the ultrasonic detection of rebar corrosion using poro-elastic model.

3.2 Poro-Elastic Acoustic Model Parameters

A complete theory of propagation of acoustic waves in fluid saturated porous media (such as sediments and concrete) was first developed by Biot (Biot, 1941; Biot, 1956a; Biot, 1956b; Biot, 1962). Starting with a general theory of three-dimensional consolidation of porous media, he applied his research to acoustic waves propagation at low and high frequencies. A generalized theory of acoustic propagation in porous dissipative media followed a few years later. Physically, a saturated porous medium consists in a porous assemblage of grains (in this case the mixture of cementite, sand and coarse) called the skeletal frame, whose interconnected pores are filled with water, the pore fluid, and usually a small amount of gas, which is often neglected. By adjusting the parameters governing the Biot model, the propagation of sound in concrete can also be modeled. Figure 3 shows a representation of the reinforced concrete model used at present in this research.

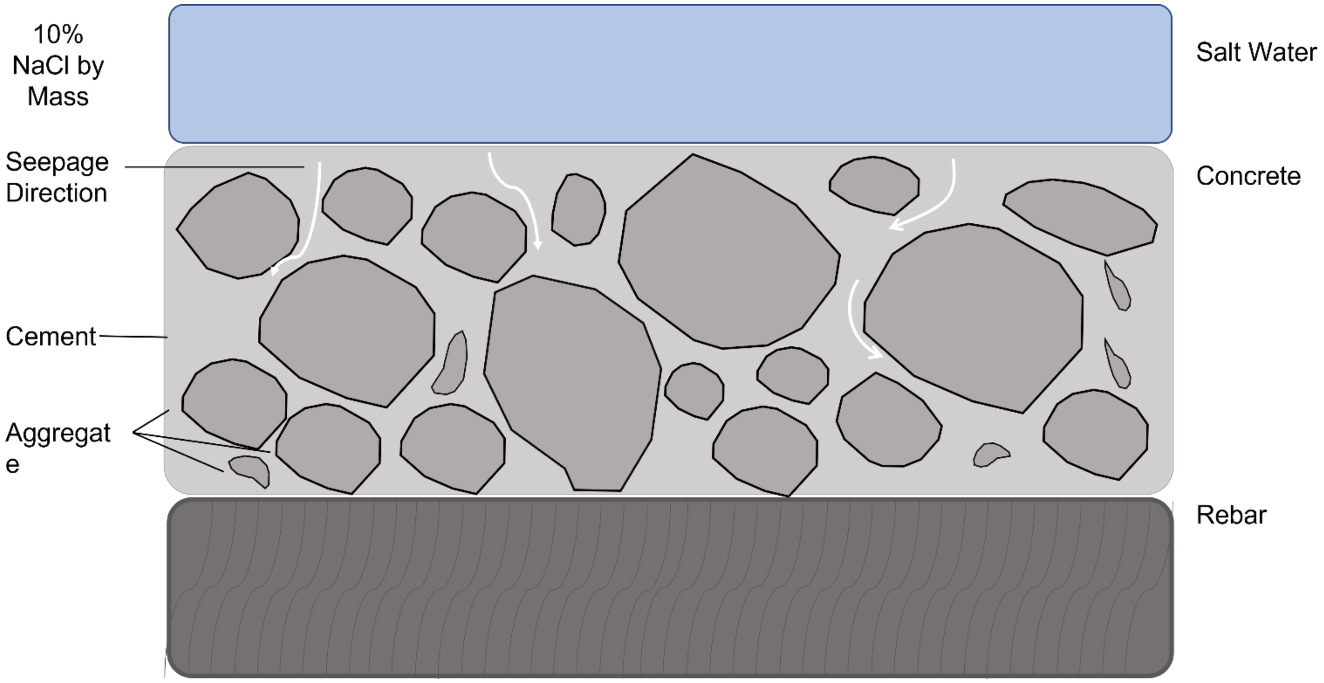

Figure 3. Poro-elastic model for a submerged reinforced concrete block.

The Biot model treats both the individual and coupled behavior of both frame and pore fluid when excited by acoustic waves. The energy loss is expected to be caused by the viscosity of the pore fluid as it moves relatively to the frame. The model predicts that the sound speed, the attenuation, and the angle of refraction of the incident acoustic wave will depend on frequency, on the elastic properties of the grains and pore fluid, on porosity, mean grain size, permeability and effective stress within the porous medium. Usually, fourteen parameters are required to describe completely the porous medium and to use the Biot model (Table I). The description of these geotechnical parameters is given in Stoll (Stoll, 1977; Stoll, 1989).

The main difficulty with the Biot and Biot-Stoll models is the number of parameters required. Fortunately, many studies concerning their applicability have been completed (Beebe et al. 1982). Also, Hovem

(Hovem et al., 1979) studied the acoustic waves to infer the pore size parameter a_p and the structure factor a from different geophysical properties of porous media. Assuming uniform spherical grains, the pore size parameter is:

$$a_p = \frac{\beta d}{3(1-\beta)} \tag{1}$$

Table I. Original Biot-Stoll model parameters.

Category	Description	Symbol	Units
Grain Properties			
	Grain Bulk Modulus	K_r	[Pa]
	Grain Mass Density	ρ_r	[kg/m^3]
Pore Fluid Properties			
	Fluid Mass Density	ρ_f	[kg/m^3]
	Fluid Bulk Modulus	K_f	[Pa]
	Fluid Viscosity	η	[kg/m.s]
Frame Properties			
	Structure Factor	α	[non-dimensional]
	Porosity	β	[non-dimensional]
	Permeability	$\varkappa$	[m^2]
	Pore Size Parameter	a_p	[m]
	Dry Frame Shear Modulus	μ	[Pa]
	Dry Frame Bulk Modulus	K_b	[Pa]
	Mean Grain Diameter	d	[m]
	Shear Logarithmic Decrement	δ_s	[non-dimensional]
	Bulk Logarithmic Decrement	δ_p	[non-dimensional]

Stoll (Stoll, 1989) studied the variation of the structure factor α as a function of frequency for different kinds of porous media. In the worst case of randomly oriented ducts, corresponding to poorly graded coarse sands, α can be as high as 3. Generally, $1 \leq \alpha \leq 3$. The frame moduli may be deduced from empirical relations or computed from the self-consistent theory of composites introduced by Berryman (Berryman, 1980). Hamilton (Hamilton, 1989) derived the following regression formula:

$$ln(Re\{K_b\}) = K_{b_0} - \beta K_{b_1} \tag{2}$$

Given the compressional bulk modulus of the porous medium, the shear modulus can be expressed as:

$$Re\{\mu_b\} = 3K_b \frac{(1-2\sigma)}{2(1+\sigma)} \tag{3}$$

where Poisson's ratio is found in the literature. The determination of the logarithmic decrements is usually found experimentally. Typically, δs ≥ δp due to the higher attenuation of the shear waves as compared with the compressional waves of the first kind. From these, the imaginary part of the bulk modulus and shear modulus can be determined:

$$Im\{K_b\} = \delta_p \frac{Re(K_b)}{\pi} \tag{4}$$

$$Im\{\mu_b\} = \delta_s \frac{Re(\mu_b)}{\pi} \tag{5}$$

3.3 Poro-Elastic Acoustic Model

We define $\vec{u}$ as the displacement of the frame, and $\vec{U}$ is the displacement of the pore fluid relative to the frame. The dilatation of an element of volume attached to the frame is:

$$e = \nabla.\vec{u} \tag{6}$$

The volume of fluid that has flowed into or out of this element is:

$$\zeta = \beta\nabla.(\vec{u} - \vec{U}) \tag{7}$$

Biot (Biot, 1956a; Biot, 1956b) proposed the following equations to be constitutive equations for a porous, saturated, isotropic medium:

$$\tau_{ij} = 2\mu e_{ij} + \delta_{ij}\big((H - 2\mu)e - C\zeta\big) \tag{8}$$

$$P = M\zeta - Ce \tag{9}$$

where τ_{ij} and e_{ij} are the stress and strain components, respectively, of an element of volume attached to the skeletal frame, P is the pore fluid pressure and μ is the shear modulus.

To understand the meaning of H, C and M and the origin of these two equations, let's consider the case where the fluid cannot move relatively to the frame, i.e. when the permeability $\varkappa$ is extremely small and the pore size is much smaller than the acoustic wave- length. Then, the equations of motion for a visco-elastic medium are obtained:

$$\tau_{ij} = 2\mu e_{ij} + \lambda e \delta_{ij} \tag{10}$$

On the other hand, if the fluid can move with respect to the frame, some coupling terms must be added, and an equation has to be created concerning the pore fluid. Thus, H, C and M are introduced. H^{-1} is the compressibility of the grain frame for a change in water pressure, while M^{-1} corresponds to the ratio of the volume of water remaining in the pores to the external pressure $-P$. The product Ce corresponds to the reaction of the grain frame on the pore fluid due to the deformation of the skeletal frame:

$$Ce = P - M\zeta \tag{11}$$

From the stress-strain equations, Biot (Biot, 1956a; Biot, 1956b) derived two equations of motion for compressional waves and one for shear waves. For compressional waves, the equations are:

$$\nabla^2(He - C\zeta) = \frac{d^2}{dt^2}\left(\rho e - \rho_f\zeta\right) \tag{12}$$

$$\nabla^2(Ce - M\zeta) = \frac{d^2}{dt^2}\left(\rho_f e - m\zeta\right) - \frac{\eta F}{\kappa}\frac{d\zeta}{dt} \tag{13}$$

Where ρ is the averaged mass density of the element of volume:

$$\rho = \beta\rho_f - (1-\beta)\rho_r \tag{14}$$

The added mass coefficient m is defined as:

$$m = \frac{\alpha\rho_f}{\beta} \tag{15}$$

F is the Biot complex correction factor. In the Biot theory, only a part of the pore fluid moves in the direction of the macroscopic gradient of pressure because of the tortuous, multi-directional nature of the pores. Therefore, less fluid flows in and out of an element of the skeletal frame for a given acceleration than if all the pores were uniform and parallel to the gradient. As a result, an apparent mass m is introduced in replacement of the real mass of fluid contained within the pores.

Two kinds of viscous damping have been taken into account by Biot: (i) the viscous resistance to fluid flow, which needs to be frequency dependent, because the fluid behavior depends on the wavelength to pore size ratio; (ii) the local viscous losses occurring in the fluid as a result of local motion near the intergranular contacts.

$$F_{viscous} = -\frac{\eta F d\zeta}{\kappa dt} \tag{16}$$

$$F(K) = F_r(K) + iF_i(K) = \frac{1}{4}\left[\frac{KT(K)}{1-\frac{2T(K)}{iK}}\right] \tag{17}$$

$$T(K) = \frac{ber'(K)+ibei'(K)}{ber(K)+ibei(K)} \tag{18}$$

$$K = a_p\left(\frac{\omega\rho_f}{\eta}\right)^{\frac{1}{2}} \tag{19}$$

Biot (Biot, 1956a) proved this function, initially developed to fit cylindrical ducts, to be accurate enough to fit two-dimensional ducts also. ω is the angular frequency. The functions *ber*(K) and *bei*(K) are the real and imaginary parts of the Kelvin function (Abramowitz et al., 1970):

$$ber(K) + ibei(K) = J_0\left(Ke^{3j\frac{\pi}{4}}\right) \tag{20}$$

$$ber'(K) = \frac{[Re(J_1\left(Ke^{3i\frac{\pi}{4}}\right) + Im(J_1\left(Ke^{3i\frac{\pi}{4}}\right)]}{\sqrt{2}} \tag{21}$$

$$bei'(K) = \frac{[-Re(J_1\left(Ke^{3i\frac{\pi}{4}}\right) + Im(J_1\left(Ke^{3i\frac{\pi}{4}}\right)]}{\sqrt{2}} \tag{22}$$

The Biot model also predicts that three kinds of acoustic wave propagate through the concrete. The compressional wave dispersion equation is:

$$(Hl^2 - \rho\omega^2)\left(m\omega^2 - Ml^2 - \frac{i\omega F\eta}{K}\right) - (\rho_f\omega^2 - Cl^2)(Cl^2 - \rho_f\omega^2) = 0 \tag{23}$$

Where l is the acoustic wavenumber. The two roots, l_1 and l_2 , are the complex wavenumbers of two compressional waves. The first one is called compressional wave of the first kind or fast wave and corresponds to the usual high velocity sound wave obtained in the elastic and visco-elastic models. The second one, called compressional wave of the second kind or slow wave, has a low phase velocity and a high attenuation. These waves are depicted in Figure 4.

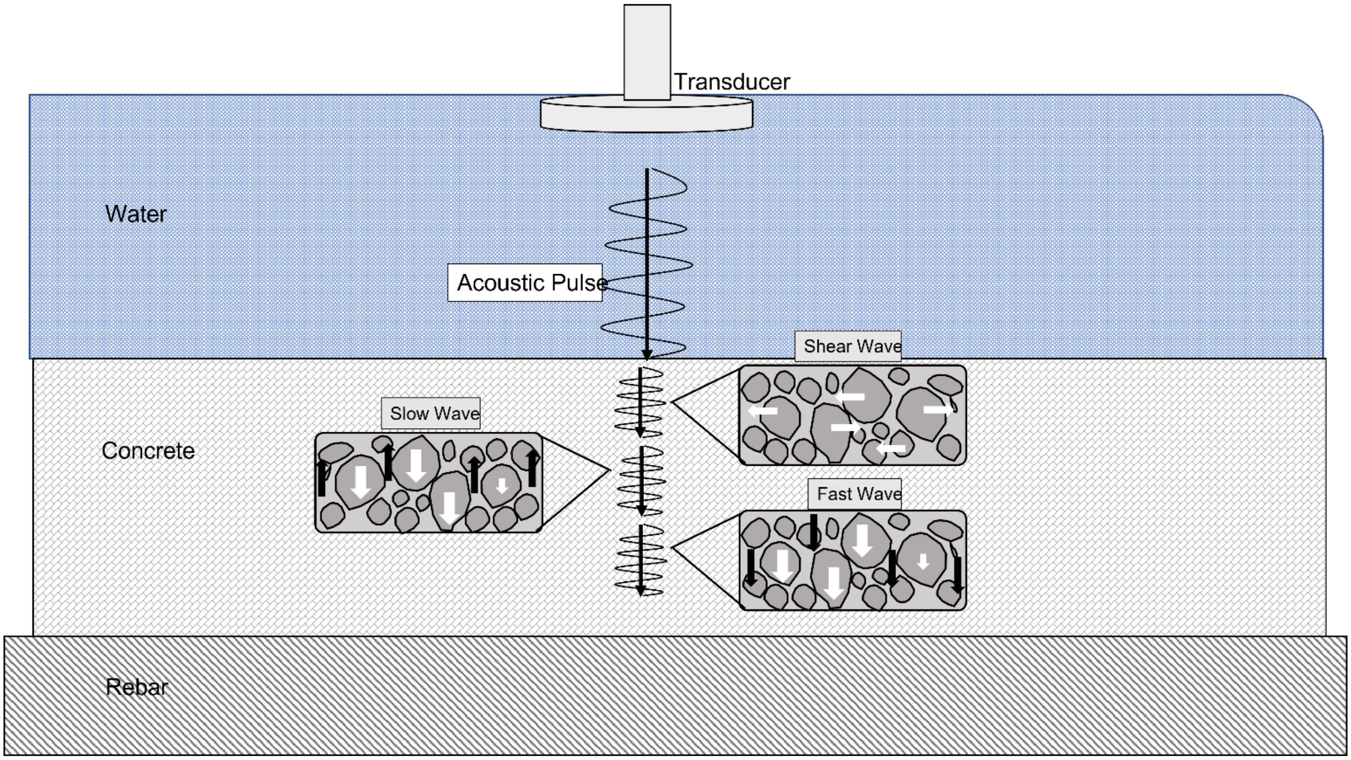

Figure 4. Acoustic wave propagation in the concrete block according to the poro-elastic model.

The shear wave dispersion equation is:

$$(\rho\omega^2 - \mu l^2)\left(m\omega^2 - \frac{i\omega F\eta}{K}\right) - \left(\rho_f\omega^2\right)^2 = 0 \quad (24)$$

This equation produces a single root, which is the shear wave number l_s . It means that only one kind of rotational wave or shear waves exists, highly attenuated and propagating at low speed. Experimentally, Plona (Plona, 1980) has proved the existence of these three waves.

The displacement potential for the incident wave in the water half-space is:

$$\Phi_1 = \left[e^{-il_1 z} + R_b e^{il_1 z}\right]e^{-i\omega t} \quad (33)$$

In the concrete layer, the scalar and vector displacement potentials are:

$$\Phi_{2,s1} = \left[A_{2,1}e^{-il_{2,1}z} + B_{2,1}e^{il_{2,1}z}\right]e^{-i\omega t} \quad (34)$$

$$\Phi_{2,s2} = \left[A_{2,2}e^{-il_{2,2}z} + B_{2,2}e^{il_{2,2}z}\right]e^{-i\omega t} \quad (35)$$

$$\Psi_{2,s} = \left[A_{2,3}e^{-il_{2,3}z}\right]e^{-i\omega t} \quad (36)$$

$$\Phi_{2,s} = \Phi_{2,s1} + \Phi_{2,s2} \quad (37)$$

$$\Phi_{2,f} = \delta_{2,1}\Phi_{2,s1} + \delta_{2,2}\Phi_{2,s2} \quad (38)$$

$$\delta_{2,1} = \frac{Hl_{2,1}^2 - \rho_s\omega^2}{Cl_{2,1}^2 - \rho_f\omega^2} \quad (39)$$

$$\delta_{2,1} = \frac{Hl_{2,2}^2 - \rho_s\omega^2}{Cl_{2,2}^2 - \rho_f\omega^2} \quad (40)$$

$$\rho_s = \rho_r(1-\beta) + \rho_f\beta \quad (41)$$

In the rebar, the scalar and vector displacement potentials are:

$$\Phi_{3,s1} = \left[A_{3,1}e^{-il_{3,1}(z+h)}\right]e^{-i\omega t} \quad (39)$$

$$\Phi_{3,s2} = \left[A_{3,2}e^{-il_{3,2}(z+h)}\right]e^{-i\omega t} \quad (40)$$

$$\Psi_{3,s} = \left[A_{3,3}e^{-il_{3,3}(z+h)}\right]e^{-i\omega t} \quad (41)$$

The displacement potential in the fluid is related to the acoustic pressure and to the particle displacement by the relations:

$$\vec{U} = \nabla\Phi \quad (48)$$

$$p = -\rho\frac{\partial^2\Phi}{\partial t^2} \quad (49)$$

In the concrete layer(s), the skeletal frame and the pore water are strained because of the propagating waves. ζ represents the volumetric strain of the pore fluid, while θ represents the volumetric strain of the skeletal frame. They can be expressed as functions of the displacement potentials:

$$\zeta = \nabla^2 \Phi_f \tag{50}$$

$$\theta = \nabla^2 \Phi_s \tag{51}$$

There are two kinds of particle displacements within the N concrete layers: the displacement of the skeletal frame and the displacement of the pore fluid. They are related to the displacement potentials respectively by:

$$\vec{u} = \nabla \Phi_s + \nabla \times \Psi_s \tag{52}$$

$$\vec{V} = \nabla \Phi_f \tag{53}$$

Because of the dual structure of concrete, several kinds of stress also exist: the compression of the skeletal frame, the shear of the skeletal frame and the pore water pressure. They are respectively related to the volumetric strains by:

$$p_{ZZ} = H\theta - 2\mu \frac{\partial u_x}{\partial x} - C\zeta \tag{54}$$

$$p_{z\mathrm{r}} = \mu \left(\frac{\partial u_x}{\partial z} + \frac{\partial u_Z}{\partial x} \right) \tag{55}$$

$$p_f = M\zeta - C\theta \tag{56}$$

H,M,C are the Biot coefficients and μ is the shear modulus. The rebar is assumed to be an elastic medium. Therefore, the relation between the displacement potentials, the acoustic pressure and the particle displacement are:

$$\vec{u} = \nabla \Phi \tag{57}$$

$$p = -\rho \frac{\partial^2 \Phi}{\partial t^2} \tag{58}$$

If the medium is modeled as a homogeneous fluid half-space on top of N-2 homogeneous concrete layers (in our case $N = 1$), with an elastic rebar at the bottom, then $4N$-6 boundary conditions are needed so that the problem be solvable. They are found using the continuity of the particle displacement and the stress equilibrium on both sides of each interface. The boundary conditions at the water-top layer interface, located at $z = -h_1$, are:

$$U_{1,z} = u_{2,z} - V_{2,z} \tag{59}$$

$$-p_1 = p_{2,zz} \tag{60}$$

$$p_1 = p_{2,f} \tag{61}$$

At each concrete-concrete layer interface, located at $z = -h_{m-1}$ (m=3,..,N-1), the boundary conditions are:

$$u_{m-1,z} = u_{m,z} \tag{62}$$

$$u_{m-1,z} - V_{m-1,z} = u_{mz} - V_{m,z} \tag{63}$$

$$p_{m-1,zz} = p_{m,zz} \tag{64}$$

$$p_{m-1,f} = p_{m,f} \tag{65}$$

Finally, at the bottom concrete layer-rebar interface, located at $z = -h_{N\text{-}1}$, the boundary conditions are:

$$u_{N-1,z} = u_{N,z} \tag{66}$$

$$u_{N-1,z} - V_{N-1,z} = u_{N,z} \tag{67}$$

$$p_{N-1,zz} = p_{N,zz} \tag{68}$$

The $4N$-6 (in our case $N = 3$) boundary conditions obtained can be sorted out in two groups. The emitted acoustic field is assumed to be known. Therefore, the set of boundary conditions at the water-top layer interface contains some known parameters: u_1, particle displacement at $z=-h_1$, and p_1, acoustic pressure at the same depth.

The second group contains only the parameters to be determined, which correspond to the amplitude of the different displacement potentials in the layers and in the bedrock, and to the reflection coefficient at the top layer-water interface. The propagator matrix [$\boldsymbol{X}$] relates the vectors representing these two groups:

$$[\boldsymbol{X}]\begin{Bmatrix} A_{21} \\ B_{21} \\ A_{22} \\ B_{22} \\ A_{31} \\ B_{32} \\ \cdots \\ A_{M1} \\ R_b \end{Bmatrix} = \begin{Bmatrix} A_0 \\ B_0 \\ C_0 \\ 0 \\ 0 \\ 0 \\ \cdots \\ 0 \\ 0 \end{Bmatrix} \tag{69}$$

The propagator matrix terms are:

$$X_{1,1} = -il_{2,1}\left(1 - \delta_{2,1}\right) \tag{70}$$

$$X_{2,1} = -Hl_{2,1}^2 + \mathrm{C}\delta_{2,1}l_{2,1}^2 \tag{71}$$

$$X_{3,1} = -M\delta_{2,1}l_{2,1}^2 + \mathrm{C}l_{2,1}^2 \tag{72}$$

$$X_{4,1} = -il_{2,1}e^{-il_{2.1}(h_1-h_2)} \tag{73}$$

$$X_{5,1} = -il_{2,1}e^{-il_{21}(h_1-h_2)}\left(1 - \delta_{2,1}\right) \tag{74}$$

$$X_{6,1} = \left(-H + C\delta_{2,1}\right)l_{2,1}^2e^{-il_{21}(h_1-h_2)} \tag{75}$$

$$X_{1,2} = il_{2,1}\left(1 - \delta_{2,1}\right)e^{il_{2,1}(h_2 - h_1)} \tag{76}$$

$$X_{2,2} = \left(-H + C\delta_{2,1}\right)l_{2,1}^2 e^{il_{2,1}(h_2 - h_1)} \tag{77}$$

$$X_{3,2} = \left(-M\delta_{2,1} + C\right)l_{2,1}^2 e^{il_{2,1}(h_2 - h_1)} \tag{78}$$

$$X_{4,2} = il_{2,1} \tag{79}$$

$$X_{5,2} = il_{2,1}\left(1 - \delta_{2,1}\right) \tag{80}$$

$$X_{6,2} = \left(-H + C\delta_{2,1}\right)l_{2,1}^2 \tag{81}$$

$$X_{1,3} = -il_{2,2}\left(1 - \delta_{2,2}\right) \tag{82}$$

$$X_{2,3} = -Hl_{2,2}^2 + C\delta_{2,2}l_{2,2}^2 \tag{83}$$

$$X_{3,3} = -M\delta_{2,2}l_{2,2}^2 + Cl_{2,2}^2 \tag{84}$$

$$X_{4,3} = -il_{2,2}e^{-il_{22}(h_1 - h_2)} \tag{85}$$

$$X_{5,3} = -il_{2,2}e^{-il_{22}(h_1 - h_2)}\left(1 - \delta_{2,2}\right) \tag{86}$$

$$X_{6,3} = \left(-H + C\delta_{2,2}\right)l_{2,2}^2 e^{-il_{22}(h_1 - h_2)} \tag{87}$$

$$X_{1,4} = il_{2,2}\left(1 - \delta_{2,2}\right)e^{il_{2,2}(h_2 - h_1)} \tag{88}$$

$$X_{2,4} = \left(-H + C\delta_{2,2}\right)l_{2,2}^2 e^{il_{22}(h_2 - h_1)} \tag{89}$$

$$X_{3,4} = \left(-M\delta_{2,2} + C\right)l_{2,2}^2 e^{il_{22}(h_2 - h_1)} \tag{90}$$

$$X_{4,4} = il_{2,2} \tag{91}$$

$$X_{5,4} = il_{2,2}\left(1 - \delta_{2,2}\right) \tag{92}$$

$$X_{6,4} = \left(-H + C\delta_{2,2}\right)l_{2,2}^2 \tag{93}$$

$$X_{l,5} = 0,\ l = 1, \dots, 3 \tag{94}$$

$$X_{4,5} = -il_{2,1} \tag{95}$$

$$X_{5,5} = 0 \tag{96}$$

$$X_{6,5} = -\rho\omega^2 \tag{97}$$

$$X_{1,6} = -i\frac{\omega}{c_f} \tag{98}$$

$$X_{2,6} = \rho_f\omega^2 \tag{99}$$

$$X_{3,6} = -\rho_f\omega^2 \tag{100}$$

$$X_{l,6} = 0,\ l = 4, \dots, 6 \tag{101}$$

The solution vector is:

$$A_0 = -i\frac{\omega}{c_f} \tag{102}$$

$$B_0 = -\rho_f \omega^2 \tag{103}$$

$$C_0 = \rho_f \omega^2 \tag{104}$$

$R_b(f)$ is found using

$$\begin{Bmatrix} A_{21} \\ B_{21} \\ A_{22} \\ B_{22} \\ A_{31} \\ B_{32} \\ \cdots \\ A_{M1} \\ R_b \end{Bmatrix} = [\boldsymbol{X}]^{-1} \begin{Bmatrix} A_0 \\ B_0 \\ C_0 \\ 0 \\ 0 \\ 0 \\ \cdots \\ 0 \\ 0 \end{Bmatrix} \tag{105}$$

The pressure reflection coefficient is a complex value calculated as a function of frequency *f*. Knowing the spectrum *S*(*f*) of the signal incident to the seafloor (in our case a time-gated impulse), the reflected spectrum becomes $R_p(f)S(f)$. The spectrum of the compressed reflected impulse is the product $R_p(f)|S(f)|^2$ gated between 0 Hz and the Nyquist frequency. An inverse Fourier Transform of this spectrum produces the compressed reflected signal *r*(*t*), which is the complex envelope of the reflected impulse.

3.4 Nonlinear Parameter Optimization

Trust-Region Reflective (TRR) algorithm: A non-linear solver using the Trust-Region Reflective (TRR) algorithm is used to match a set of synthetic data to the Biot-Stoll model. Synthetic data is produced separately using set values in a script that functions purely as a table of constants. The synthetic pulse is then fed these constants and uses the Biot model for sound propagation in a porous medium to create a fake signal that the model can be ran against to test for accuracy.
The TRR method of optimization and data fitting uses an objective function *f* which takes *n* arguments and returns a scaler. The objective function is defined by the user and relates a set of *m* data points (of the form (*x*,*y*)) and a model function φ that relates the points by a set of n parameters β where $m \geq n$:

$$f = \sum_{i=1}^{m}(y_i - \varphi(x_i, \beta))^2 \tag{106}$$

The goal of the algorithm is to minimize the objective function by altering the parameters so as to get the smallest value of f for all m. In the case of this research, the model function is the Biot-Stoll model with a subset of the constants in the Biot-Stoll model representing the free parameters in the model function. The TRR approach does this by minimizing a function *q* which adequately approximates *f* in a specific trust region *N*. A trial step, *s*, is calculated such that:

$$\min_{s}\{q(s), s \in N\} \tag{107}$$

The point $x+s$ is retained if $f(x+s) < f(x)$. Meaning that the new point is accepted if it reduces the value of the optimization function.

The specific calculations of q, s, and the rules for updating N are what define the particularities of any given trust region method. The MATLAB function *lsqnonlin* uses a TRR method employing preconditioned conjugate gradients, where each iteration of the objective function is approximated as the solution to a series of linear equations. Additionally, the nonlinear solver built into MATLAB uses what is called a subspace trust-region method wherein the trust-region is restricted to a two-dimensional subspace S. Minimizing the two-dimensional case is much simpler and therefore all that is needed to find basis vectors for S which are defined to be in the direction of the gradient and in the direction of negative curvature. The main steps taken when optimizing a nonlinear least squares problem using the TRR method are as follows:

1. Find the two-dimensional subspace, S, of the trust region N.
2. Solve the following to find trial step size: min $\{\frac{1}{2}s^T Hs + s^T \nabla \ni \left|\left|Ds\right|\right| < \lambda\}$ where λ is the scaling factor and Ds is the scaling matrix.
3. If $f(x+s) < f(x)$ then $x = x$+s, else increase the trust-region dimension and size by some constant amount.
4. Adjust λ.

This process is repeated until the algorithm minimizes the objective function past the function tolerance specified in the problem.

Levenberg-Marquardt Algorithm: The Levenberg-Marquardt Algorithm works in a similar way to the TRR and is another option for non-linear least squares data fitting. The LMA is set up the same way by minimizing the sum of the squares of the residuals of the objective function:

$$f = \sum_{i=1}^{m}(y_i - \varphi(x_i, \beta))^2 \tag{108}$$

The main difference between the trust region and the LM algorithms is that the LMA adapts the update criteria λ based off the objective function. As the objective function is minimized, the successive steps taken by the algorithm get smaller and smaller, so they converge more quickly on a minimum. In this regard, the LMA can be thought of as switching between gradient-descent and Gauss-Newton methods depending on the change in the objective function.

For these reasons, the LMA is a common choice in non-linear model fitting; however, when compared to the TRR on the Biot-Stoll model, the TRR performed better. The TRR approach converged more slowly than the LMA, however the TRR converged to more optimal solutions (the parameter values were closer to the actual values than they were in the LMA) and had better first order optimality than did the LMA. With this in mind, the TRR was selected for the analysis of the data collected for this project.

Chapter 4. Results and Discussion

4.1 Year 1 - Initial Concrete Sample Modeling and Experimentation

In the initial phase of the project, the investigator focused his effort on the modeling and acoustic analysis of a specific concrete sample provided by Dr. Presuel Moreno Using this sample, the following work has been completed:

- Development and testing of the poro-elastic model for the reinforced concrete samples.
- Ultrasonic data collection on a limited number of reinforced concrete samples. The concrete block sample was submerged in salt water in a small tank. An Olympus Panametrics V389, operated at 500 [kHz] and connected to an HP8112A high-frequency impulse generator and a Tektronix DPO3014, was placed at 12 [cm] above the concrete surface, to avoid near-field acoustic interferences (Figure 5).
- A sample of experimental results is shown in Figure 6. The transducer was carefully placed on top of the corroded rebar and moved along the axis of the rebar in increments of 0.5 [cm]. The initial position was at 2.5 [cm] off the edge of the concrete block. The last position was at 9.5 [cm] off the edge of the concrete block. At every position, ten acoustic signatures were recorded. In order to reduce the electric and thermal noise contained in the high-frequency measurements, an acoustic signature averaged across the ten measurements was computed (Figure 7).
- Processing of simulated data sets and comparison between simulated and measured data were completed. Figure 8 shows an example of measured vs. simulated acoustic signatures, using the parameters listed in Table II. The table coefficients were obtained from concrete sample information provided by Dr. Presuel Moreno and from literature. The results clearly indicate that model and measurements match closely.
- Finally, the non-linear solver using Trust-Region Reflective (TRR) algorithm is under evaluation, in an attempt to match a set of synthetic data to the Biot-Stoll model. Synthetic data are produced separately using set values in a script that functions purely as a table of constants. The synthetic pulse is then fed these constants and uses the Biot model for sound propagation in a porous medium to create a fake signal that the model can be ran against to test for accuracy. As of now, the model is capable of successfully matching the parameters shown in Table III.

To clarify Figure 8, the focus is both on the surface concrete echo and on the rebar echo. There is an excellent match in amplitude and time-signature at the concrete surface between model and measurement, which indicate that the poro-elastic model uses a representative set of physical parameters.

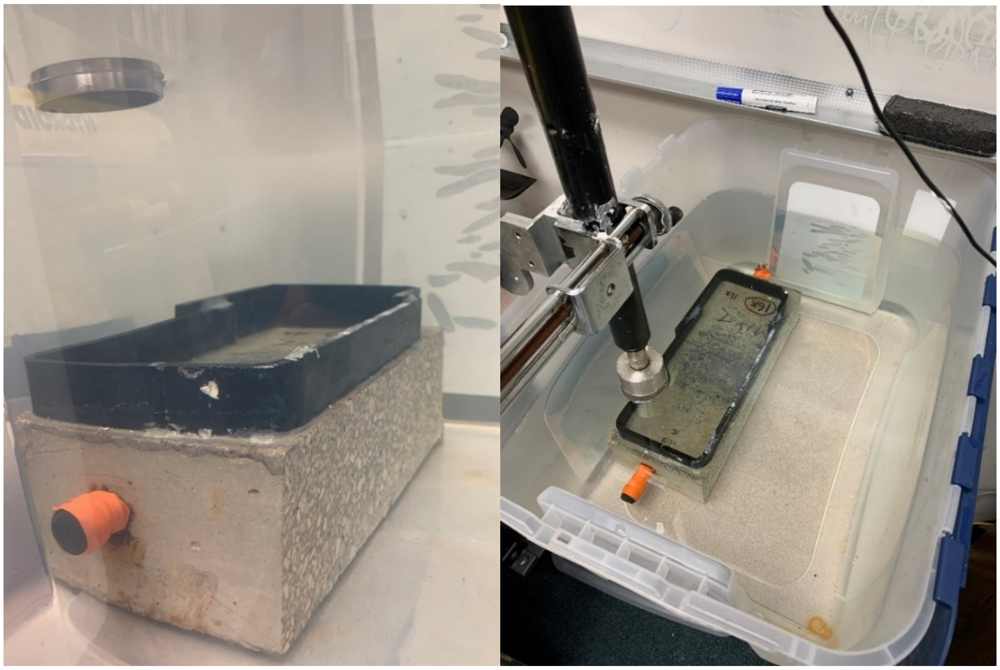

Figure 5. Ultrasonic testing of the reinforced concrete sample fully immersed in salt water. Left: side-view. Right: Top view.

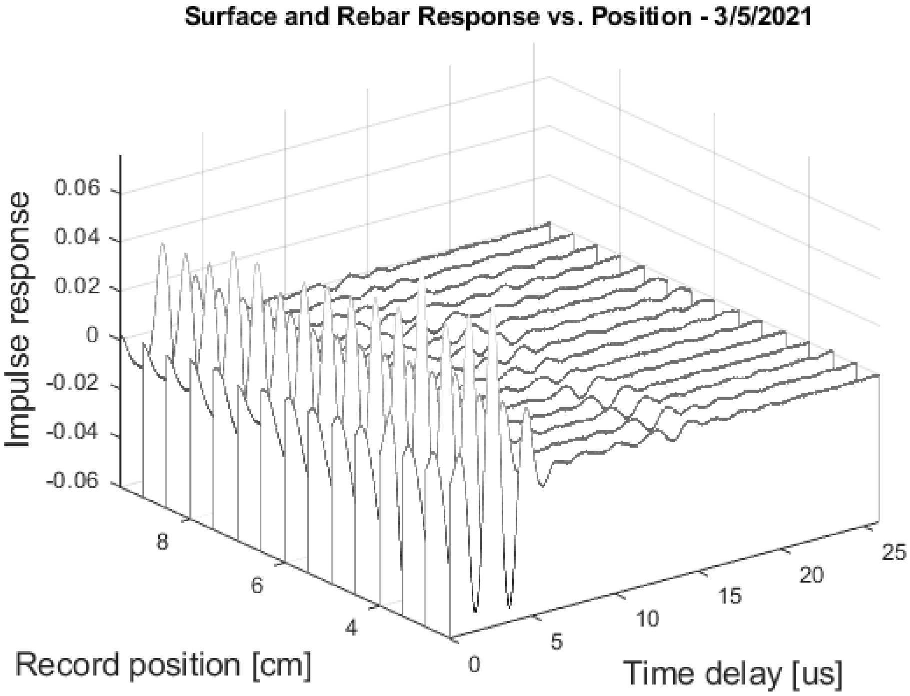

Figure 6. Waterfall plot of ten ultrasonic signatures for the tested concrete sample, measured every 0.5 [cm] from the edge of the concrete block and averaged over 10 records.

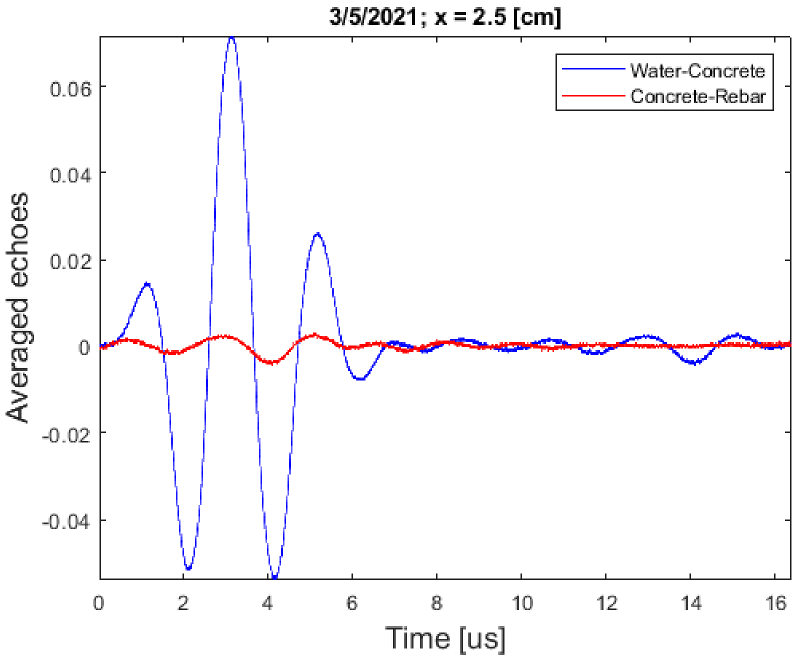

Figure 7. Overlaid concrete surface echo and rebar echo, with the transducer placed at 2.5 [cm] from the edge of the concrete block, averaged across the ten measurements (following careful time alignment).

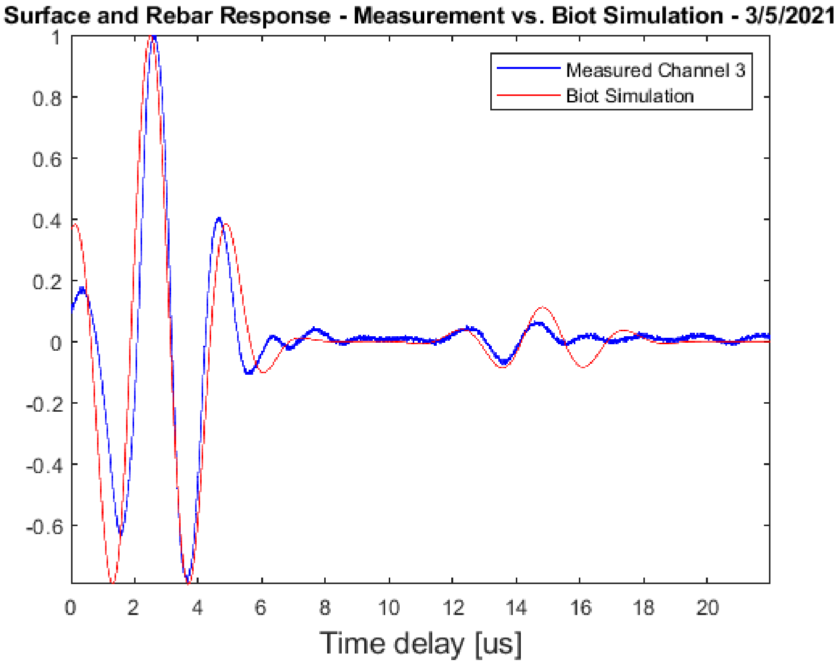

Figure 8. Comparison between measured and simulated results. In blue: concrete echo and rebar echo obtained using an average across the ten ultrasonic signatures (following careful time alignment, with the transducer placed at 2.5 [cm]. In red: Poro-elastic model simulation result for the same configuration, using the parameters listed in Table I.

Table II. Physical properties of the reinforced concrete material used in the simulation.

Layer	Physical Property	Symbol	Value
Salt water (top layer and pore fluid)	Mass density of the fluid	ρ_f	$1026\ kg/m^3$
	Phase Speed in the Fluid	c_f	$1.5 * 10^3\ m/s$
	Bulk modulus of the Pore Fluid	K_f	$2.28 * 10^9\ Pa$
Concrete: 16.6% cementite, 33.4% sand, 43.1% coarse, 6.8% water (if saturated)	Bulk modulus of the Concrete Material	K_r	$4.49 * 10^{10}\ Pa$
	Mass density of the dry concrete material	ρ_r	$2341\ kg/m^3$
	Fluid Viscosity	η	$0.001\ kg/m.s$
	Porosity	β	0.1
	Permeability	$\varkappa$	$8.0^*10^{-12}m^2$
	Pore Size Parameter	a_p	$1.3975^*10^{-5}m$
	Dry Concrete Shear Modulus	μ	$1.22 * 10^{10}Pa$
	Poisson's ratio of the Dry Concrete	ν	0.27
	Mean Grain Diameter	d	$0.0002\ m$
	Shear Logarithmic Decrement	δ_s	0.12
	Bulk Logarithmic Decrement	δ_p	0.12
	Biot Added Mass Coefficient	c	1.25
Rebar	Mass density of the Rebar	ρ_b	$7800\ kg/m^3$
	Phase Speed in the Rebar	c_b	$5180\ m/s$
	Depth below the concrete surface	h	$0.022\ m$

Table III. Error performance analysis in estimating the simulated physical properties of the reinforced concrete material using the TRR algorithm.

	Synthetic Value	Algorithm Value	Percent Error
Concrete Porosity [%]	10.0	9.93	-0.7%
Concrete Bulk Modulus [Pa]	4.488*10^10	4.4431*10^10	-1.0%
Concrete Compressional Log Decrement	0.12	0.1160	-3.3%
Concrete Shear Log Decrement	0.12	0.1231	2.6%

4.2 Year 2 - Experimentation and Analysis of New Concrete Samples

In the later stage of this year, a new set of concrete samples (shown in Figure 9), showing various degrees of cracking, has been identified for new acoustic tests. The intent is to compare the corrosion potential measurements with the acoustic measurements to establish corrosion and cracking trends in the data.

Rebar Potential Measurements: A series of rebar potential measurements was first performed to verify that corrosion is indeed taking place. A galvanostatic pulse (GP) approach was used to obtain R_s and i_{corr} , one week after the samples were placed indoors. The results are shown in Table IV. These measurements were done using a saturated calomel electrode along with a galvanostatic pulse to gather R_s and i_{corr}. Both measurements will be repeated every time new acoustic measurements are taken to quantify the corrosion of the rebar over time. In Figure 9 and Table IV, the concrete samples are numbered from left to right, where *Rebar 1* is at the top of each concrete sample. The cracks in samples two and three are a result of the corrosion of the rebar beams (2) embedded in each of the samples. Note that each rebar extended 25.4 [cm] inside the reservoir with a diameter of 1.6 [cm] yielding a surface area of 128.6 [cm^2] (including the area of the end of the rebar) that is available to corrode. Also, the samples were stored outside in marine atmosphere and brought indoors to gather the E, R_s and i_{corr} values. Before rebar potential measurements were taken, the samples were wet using a sponge and allowed to sit for some time.

Figure 9. New set of reinforce concrete samples showing various levels of cracking due to corrosion. Note that each sample contains two rebars.

Table IV. Rebar potential measurement for a new set of samples.

	Sample 1		Sample 2		Sample 3	
	Rebar 1	Rebar 2	Rebar 1	Rebar 2	Rebar 1	Rebar 2
E_{corr} [mV]	-31.10	-183.90	-159.20	-281.60	-142.20	-91.15
R_s [kΩ]	0.96	0.81	0.15	0.29	0.26	0.75
I_{corr} [μA]	54.83	29.83	326.25	348.00	381.95	313.20
i_{corr} [μA/cm^2]	0.43	0.23	2.54	2.71	2.97	2.43

In Table IV, more negative corrosion potential measurements indicate an increased likelihood of corrosion taking place within the rebar. These measurements consist of recording the potential difference between the material and a reference electrode (in this case a calomel electrode), this difference is then used to generalize the electrochemical environment of the rebar. If these measured potentials trend positive over time, then that can indicate that passivation is occurring; however, if the measurements trend negative over time than that is an indication that the corrosion rate of the rebar is increasing. It is important to note that these rebar potential measurements are localized and do not give information on the chemical kinetics of the reactions taking place. This is important to note as the corrosion of the rebar is likely highly localized and not uniform across the beam, this can be seen in the variability of the corrosion potential measurements along each of the steel rebar beams. These measurements help qualify the presence of corrosion along the rebar and are couple with galvanostatic pulse measurements to get a more complete understanding of the corrosive environment of the rebar and surrounding concrete. The corrosion current density and resistance measures are used for quantifying the rate of corrosion taking place within the concrete. i_{corr} is defined as the current density and represents the electrical current flowing through a unit cross section of the material being measured. In this case, the material being measured is the current running through the rebar as it corrodes in units of $[\frac{\mu A}{cm^2}]$. This is a helpful measure as it can be used to estimate the mass of steel loss due to corrosion; these values are standardized by the ASTM and anything above 0.1 $[\frac{\mu A}{cm^2}]$ indicates that corrosion is occurring.

Acoustic Measurements: Following this, the acoustic procedure described in section 4.1 was completed on these new samples. The data acquisition process went as follows; each reinforced concrete block has two steel rebar beams embedded inside of it. Each rebar beam extended 25.4 [cm] inside the concrete and each beam had a diameter of 1.6 [cm]. The concrete sample was then submerged in a saltwater solution (15% NaCl concentration by mass) to mimic a marine environment. All acoustic data was collected using a high-frequency, narrow beam transducer operating at 500 [kHz] connected to a high-frequency impulse generator and an oscilloscope. The transducer was placed in the water and positioned 12 [cm] above the surface of the concrete directly in line with the corroded rebar sample. The origin is 2.5 [cm] off the edge of the concrete, this is to ensure that the acoustic measurements were not hitting the edge and disrupting the signal. Measurements were taken at 5mm increments along the rebar running for 10 [cm]; at each point along the rebar 10 acoustic samples were taken. These samples were then averaged to reduce noise in the signal. After the data were averaged, the average will be given to the TRR to fit to the Biot-Model. This process was repeated for all rebar beams.

At this time, the model analysis and matching has not been completed. In year 2, these measurements will be repeated to understand the changes of the Biot parameters as the rebar corrodes. Given that all the measurements will take place along the same points of the rebar, the only variable that will be changing is the elapsed time between measurements which will reflect the corrosion of the steel beams over time. This is because as steel corrodes it expands as the iron in the rebar beams corrodes and forms iron-hydroxides which exert pressure on the surrounding concrete, leading to cracks and eventually failure of the structure if these issues are not addressed. The aim of the repetition is to establish the trends between these parameters and corrosion with the end goal being field applications.

The processing of the initial set of free parameters on the TRR solver was completed for several time-intervals. V shows the initial value of these parameters. Table VI identifies the set of parameters that were allowed to vary with the TRR solver. The initial value table coefficients were obtained from concrete sample information provided by Dr. Presuel-Moreno and from literature.

Table V. Initial physical properties of the reinforced concrete material used in the simulation.

Layer	**Physical Property**	**Symbol**	**Value**
Salt water (top layer and pore fluid)	Mass density of the fluid	ρ_f	$1026\ kg/m^3$
	Phase Speed in the Fluid	c_f	$1.5 * 10^3\ m/s$
	Bulk modulus of the Pore Fluid	K_f	$2.28 * 10^9\ Pa$
Concrete: 16.6% cementite, 33.4% sand, 43.1% coarse, 6.8% water (if saturated)	Bulk modulus of the Concrete Material	K_r	$4.49 * 10^{10}\ Pa$
	Mass density of the dry concrete material	ρ_r	$2341\ kg/m^3$
	Fluid Viscosity	η	$0.001\ kg/m.s$
	Porosity	β	0.1
	Permeability	ϰ	$8.0^*10^{-12}m^2$
	Pore Size Parameter	a_p	$1.3975^*10^{-5}m$
	Dry Concrete Shear Modulus	μ	$1.22 * 10^{10}Pa$
	Poisson’s ratio of the Dry Concrete	ν	0.27
	Mean Grain Diameter	d	$0.0002\ m$
	Shear Logarithmic Decrement	δ_s	0.12
	Bulk Logarithmic Decrement	δ_p	0.12
	Biot Added Mass Coefficient	c	1.25
Rebar	Mass density of the Rebar	ρ_b	$7800\ kg/m^3$
	Phase Speed in the Rebar	c_b	$5180\ m/s$
	Depth below the concrete surface	h	$0.022\ m$

Table VI. Initial values given to the free parameters and percentage of fluctuation allowed for lower and upper bounds as a proportional difference from the initial value.

Initial Parameter Value	**Free Parameter Bounds**
$\overrightarrow{\phi_o} = \begin{matrix} \beta = 0.10 \\ K_r = 4.488 \times 10^{10} \\ \delta_s = 0.12 \\ \delta_p = 0.12 \\ h_c = -0.05 \\ h_r = -0.072 \\ \rho_r = 7800 \end{matrix}$	$(lb, ub) = \begin{bmatrix} \beta: (0.98, 1.031) \\ K_r: (0.975, 1.01) \\ \delta_s: (0.99, 1.006) \\ \delta_p: (0.99, 1.006) \\ h_c: (1.01, 0.99) \\ h_r: (1.01, 0.99) \\ \rho_r: (0.965, 1.10) \end{bmatrix}$

Acoustic measurements have been completed at distinct time intervals to start trend analysis measurements for changes in Biot-Stoll model parameters (Table VII). However, the fluctuation range allowed for each parameter was initially kept very narrow (3.5% at the most, as shown in Table VI), in order to guaranty the numerical stability of the inversion model.

Table VII. Fluctuation in the model parameters using TRR, for the scanning of rebar 2 in sample 2.

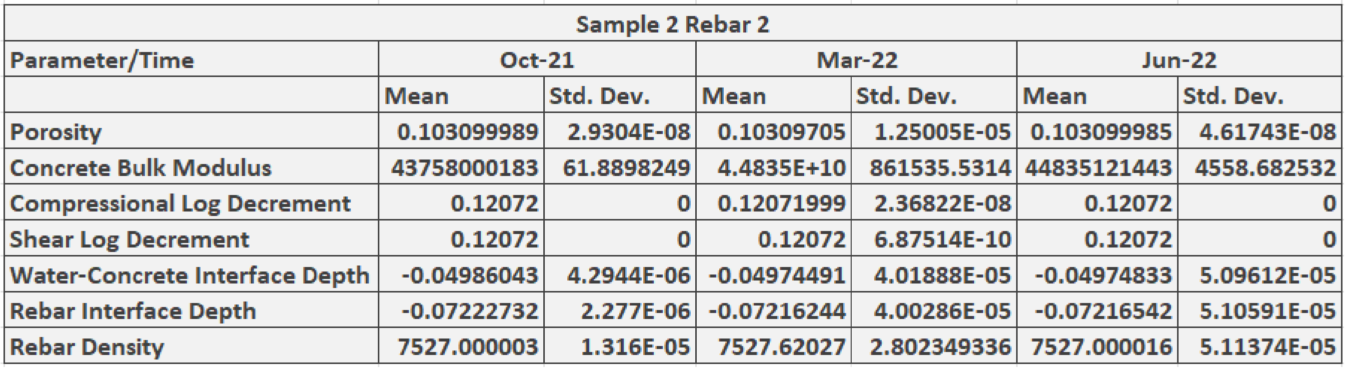

Sample 2 Rebar 2						
Parameter/Time	**Oct-21**		**Mar-22**		**Jun-22**	
	Mean	**Std. Dev.**	**Mean**	**Std. Dev.**	**Mean**	**Std. Dev.**
Porosity	0.103099989	2.9304E-08	0.10309705	1.25005E-05	0.103099985	4.61743E-08
Concrete Bulk Modulus	43758000183	61.8898249	4.4835E+10	861535.5314	44835121443	4558.682532
Compressional Log Decrement	0.12072	0	0.12071999	2.36822E-08	0.12072	0
Shear Log Decrement	0.12072	0	0.12072	6.87514E-10	0.12072	0
Water-Concrete Interface Depth	-0.04986043	4.2944E-06	-0.04974491	4.01888E-05	-0.04974833	5.09612E-05
Rebar Interface Depth	-0.07222732	2.277E-06	-0.07216244	4.00286E-05	-0.07216542	5.10591E-05
Rebar Density	7527.000003	1.316E-05	7527.62027	2.802349336	7527.000016	5.11374E-05

4.5 Year 3 - Experimentation and Analysis of Concrete Sample 16X-C with Forensic Analysis

For the year 3 effort, the ultrasonic tests were conducted on Sample 16X-C submerged in a bath containing a somewhat > 3.5% NaCl concentration. This was done to enhance the corrosion acceleration, as the sodium chloride levels in seawater typically range around 3.5%. The transducer was placed with the head partially submerged in the water and fixed (see Figure 15). The distance between the bottom of the transducer and the top of the rebar remained at 12 centimeters during all the measurements, and it was positioned vertically about the sample. The transducer was settled up above the rebar so the center of the emission cone could directly reach the intended location. Measurements were recorded across all the rebar length at regular intervals of 10 millimeters. At each location, a total of 10 measurements were meticulously preserved. This approach was adopted to mitigate any potential disruptions caused by external disturbances, ensuring the data's integrity for subsequent analysis. The length of measurements spanned from 0 [mm] to 300 [mm] to cover all the rebar length.

Figure 10. Sample 16X-C, ultrasonic experimental setup.

Data was collected using an HP 8112A pulse generator with a Tektronix MDO3024 mixed-domain oscilloscope (see Figure 16). The pulse generator was responsible for generating the signal intended for transmission by the transducer. In contrast, the Oscilloscope was utilized to gather acoustic data from the reception of echoes originating from concrete and rebar. Measurements were recorded across the complete span of the specimen, with data being gathered at regular intervals of 10 millimeters.

4.5.1 Forensic Analysis

Sample 16X-C was subjected to a forensic analysis. It was marked transversally with a permanent marker in such a way as to delimit the position to be cut, maintaining a distance of 0.3 to 0.5 cm from the rebar. After this, a wet tile saw was used to perform the cut. The cut sample is shown in Figure 11. An LED Light MIC-209 microscope was used to observe continuous zoom magnification power and clear stereo erect images regarding the points that presented signs of corrosion on the rebar.

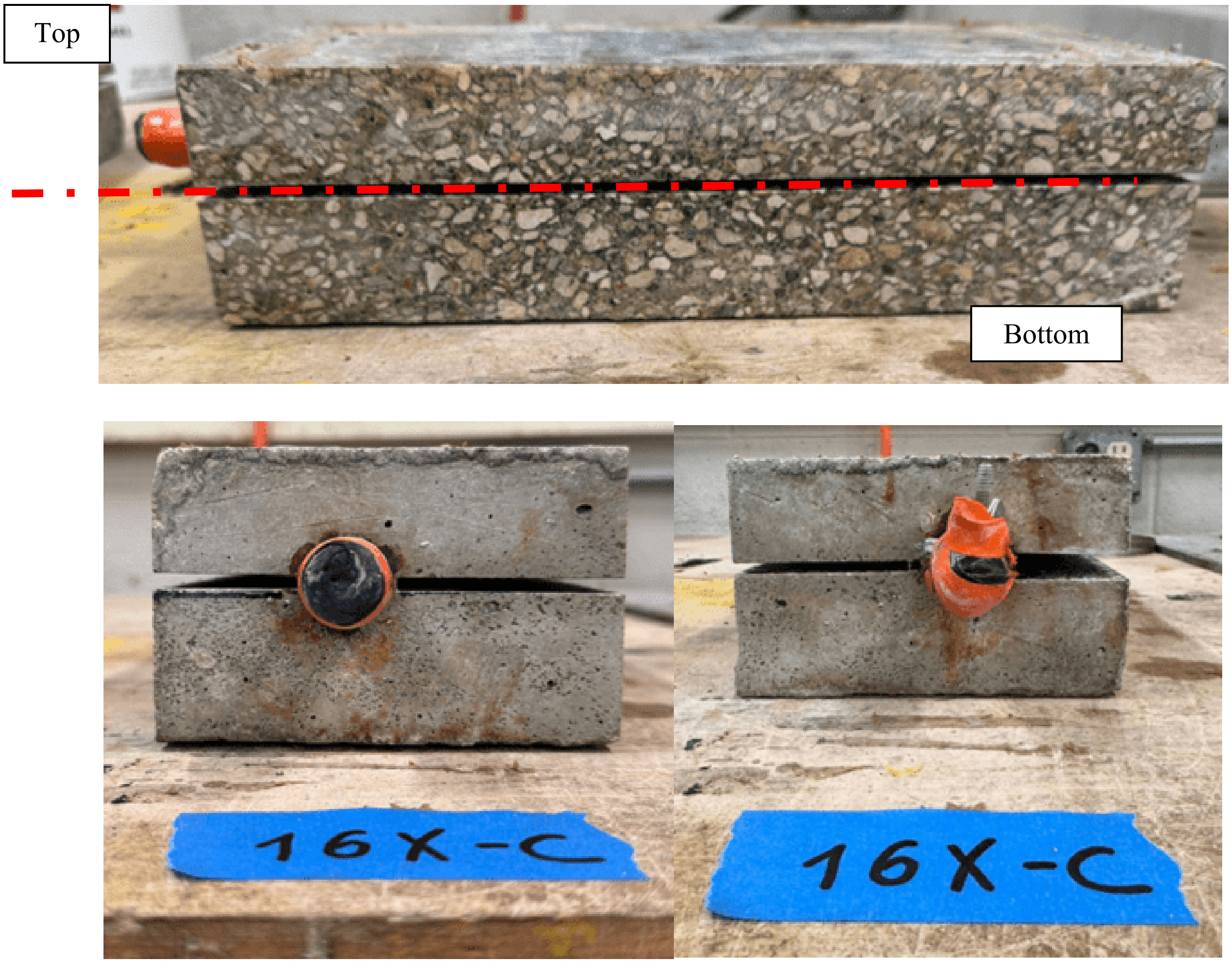

Figure 11. Final configuration after use of the wet tile saw.

4.5.2 Defining Biot-Stoll Parameters

The adapted Biot-Stoll model, employed in the proposed model, utilizes a non-linear least squares solver to simulate the surface response. Specific values must be assigned to the parameters of the Biot-Stoll model. These values are presented in Table VIII. The focus of this analysis remained on three critical parameters: Water Concrete Interface Depth, Concrete Rebar Interface Depth, and Rebar Depth Below Water in 4 different time intervals: June 2023, December 2023, February 2024 and April 2024.

Table VIII. Biot-Stoll parameter values for Sample 16X-C.

	Physical Property	**Value**	**Unit**
Sat Water	Mass Density of Fluid	1026	[kg/m3]
	Phase Speed in Fluid	1500	[m/s]
	Fluid Bulk Modulus	2.28e9	[Pa]
Concrete	Bulk Modulus of Concrete Material	4.488e10	[Pa]
	Mass Density of Dry Concrete Material	2340.9	[kg/m^3]
	Fluid Viscosity	1e-3	[kg.s/m]
	Porosity	0.1	[nd]
	Pore Size Parameter	1.3957e-5	[m]
	Dry Concrete Shear Modulus	1.224e10	[Pa]
	Permeability	8e-12	[m^2]
	Poisson's Ratio of Dry Concrete	0.27	[nd]
	Mean Grain Diameter	0.2e-3	[m]
	Shear Logarithmic Decrement	0.12	[nd]
	Bulk Logarithmic Decrement	0.12	[nd]
	Biot Added Mass Coefficient	1.25	[nd]
Rebar	Mass Density of Rebar	7800	[kg/m^3]
	Phase Speed in Rebar	5180	[m/s]
	Depth Below Concrete Surface	-0.076	[m]

4.5.3 Fitting of the Biot-Stoll Model Parameters

The depth of the water-concrete interface and the concrete-rebar interface are crucial factors in identifying corrosion in our specimens. Generally, a decrease in the water-concrete interface depth over time may suggest that the concrete surface is rising due to internal pressure within the sample. Likewise, an increase in the concrete-rebar interface depth over time indicates that the distance between the top of the rebar and the concrete surface has increased, signaling a similar scenario.

An analysis was carried out about Sample 16X-C. It was subjected to ultrasonic testing in July 2023 (data collected every 10mm along the entire length of the rebar), December 2023 (data collected every 10mm along the entire length of the rebar), February 2024 (from 60 to 90 mm), April 2024 (data collected every 10mm along the entire length of the rebar) and May 2024 (every 10mm along the entire length). After the analysis in May 2024, the sample was opened to examine the corrosion points.

Using the Biot-Stoll model combined with the Trust-Region Reflective algorithm, it was possible to collect essential parameters, which are porosity, concrete bulk modulus, compressional log decrement, shear log decrement, water concrete interface depth, concrete rebar interface depth, rebar density, mass density of fluid, phase speed in rebar and biot added mass coefficient. All these parameters were calculated for every 10mm along the entire rebar from 0mm to 300mm. Table IX shows the exact values for this analysis, and Figure 12 shows the curve behavior regarding the three parameters for the entire rebar length.

Table IX. Sample 16X-C statistical results across measurement location for June 2023 and May 2024.

Parameters	**Mean [m]**	**Standard deviation [m]**	**Variance $[m^2]$**
June 23 - Signed Transducer to Concrete Interface Depth (-h)	-0.050905885	0.002667123	7.11E-06
June 23 - Signed Transducer to Rebar Interface Depth –(d+h)	-0.076962825	0.002667608	7.12E-06
June 23 - Signed Concrete Cover (-d)	-0.02605694	0.000855661	7.32E-07
May 24 - Signed Transducer to Concrete Interface Depth (-h)	-0.050727323	0.002711179	7.35E-06
May 24 - Signed Transducer to Rebar Interface Depth –(d+h)	-0.076794669	0.002660762	7.08E-06
May 24 – Signed Concrete Cover (-d)	-0.026067346	0.001101678	1.21E-06

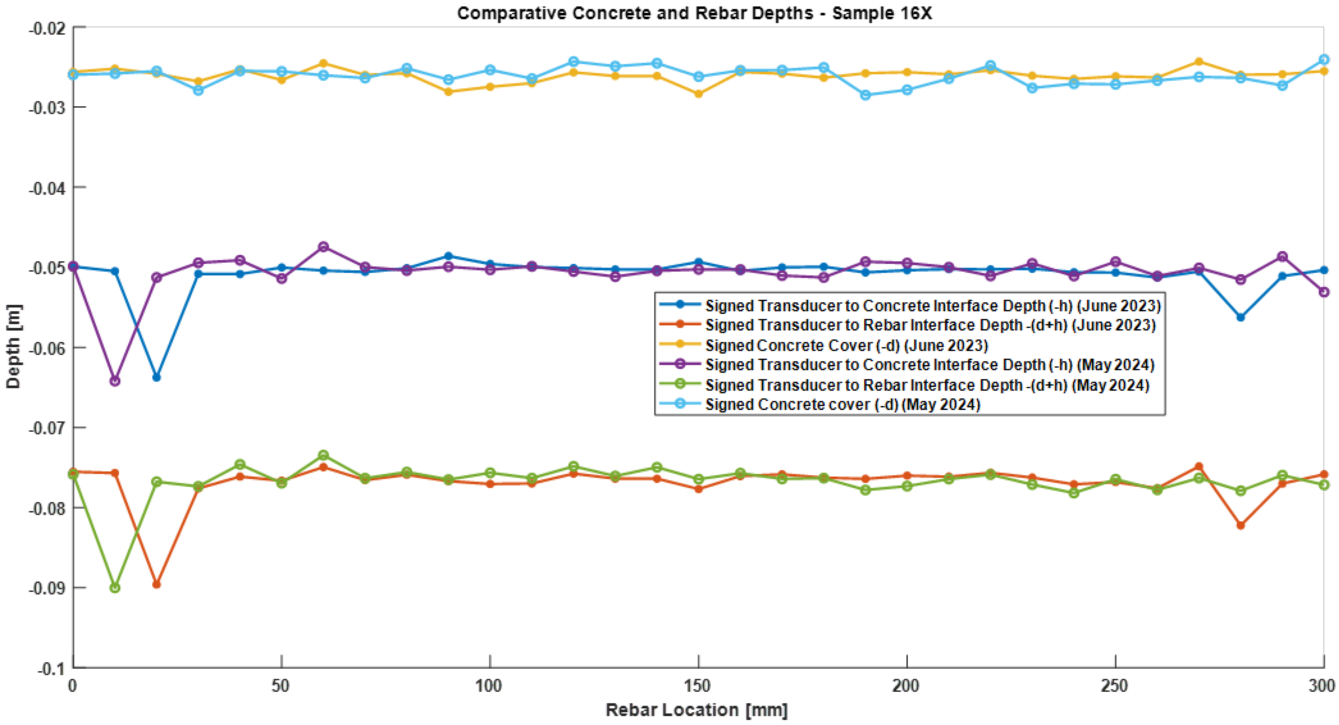

Figure 12. Signed transducer to rebar interface depth, signed transducer to concrete interface depth and signed concrete cover for Sample 16X-C rebar 1 from June 2023 to May 2024 measurement.

From Table IX, it was possible to notice a slight increase, on average, in the signed concrete cover from June 2023 to May 2024. One of the possible explanations would be the deterioration of the metal section (embedded rebar) which indicates a gradual corrosion of the rebar.

4.5.4 Forensic Analysis Observation

The forensic analyses were performed on Sample 16X-C which had a single rebar. The upper concrete image in Figures 13 and 14 shows the concrete in direct contact with the rebar, i.e., it shows the rebar trace. The bottom images show the rebar and the concrete below.

Figure 13. Sample 16X-C after the complete opening of the concrete block.

During the visual analysis, it was possible to notice that most corrosion products were located on the rebar outside the concrete. The corrosion was observed on the rebar under the tape and shrinkage wrap. It is possible to notice that after removing the tape, the rebar outside the concrete showed clear signs of corrosion despite the attempt to avoid it by using the black tape.

Figure 14. Sample 16X-C after removing the orange shrinkage wrap.

When it comes to the portion embedded, the corrosion spots are small. The section showing some signs of corrosion was on the rebar surface under the solution reservoir, no corrosion was observed on the opposite side of the rebar. Three spots, at around 20mm (about 0.79 in), 110mm (about 4.33 in), and 220 mm (about 8.66 in), showed little points of red rust. However, the rest of the rebar did not present any corrosion along the rebar length. The two first spots (20mm and 110mm) are shown in Figure 15.

Figure 15. Sample 16X-C, corrosion spots around 20 mm and 110 mm.

A stereo microscope was used to provide greater detail in these areas so that a more detailed analysis of the points that showed corrosion could be conducted. The microscope was used at two separate time intervals. Firstly, these points were analyzed before cleaning the rebar. A sandblaster was used to clean the rebar by applying abrasive walnut sand jets to remove corrosion products and concrete particles attached to the surface. After this cleaning, the rebar was examined again with the stereo microscope.

Figure 16. Sample 16X-C, corrosion pit position 220 mm with high magnification after cleaning.

Figure 16 shows the high magnification image of the spot at 220 mm after cleaning the rebar. The corrosion spot located at 220 mm was visible only with the microscope. After cleaning the rebar, the 220mm spot was the smallest among the three spots inspected with the microscope. Figure 16 shows the high magnification image of the spot at 110 mm after cleaning the rebar. A small pit was still observed after cleaning the rebar for position 110mm.

Figure 17. Sample 16X-C, corrosion pit position 110 mm with high magnification after cleaning.

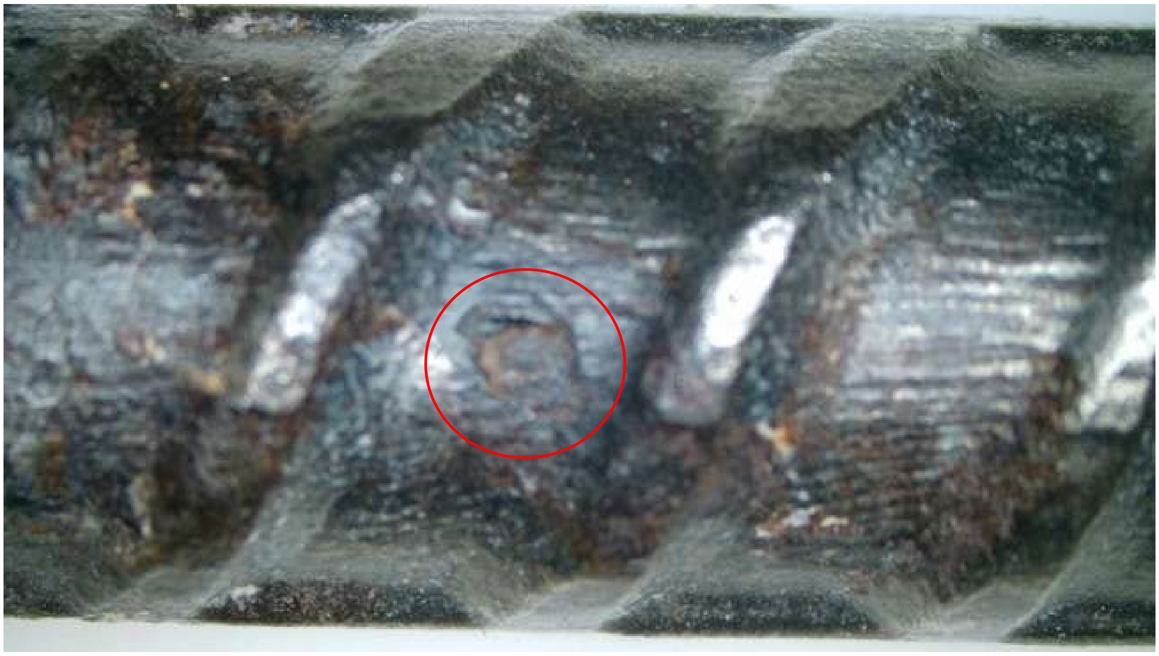

Figure 18. Sample 16X-C, corrosion pit position 20 mm after cleaning.

Analyzing the entire rebar, the point that showed the most signs of corrosion was around 20 mm. After cleaning (Figure 19), a pit arising from the corrosive process is evident. These three points could be observed on the rebar side below the reservoir. Regarding the opposite side of the rebar, before and after cleaning did not present any sign of corrosion taking place along the entire length. Both sides of the rebar are observed in Figure 20, image a top side, image b bottom side.

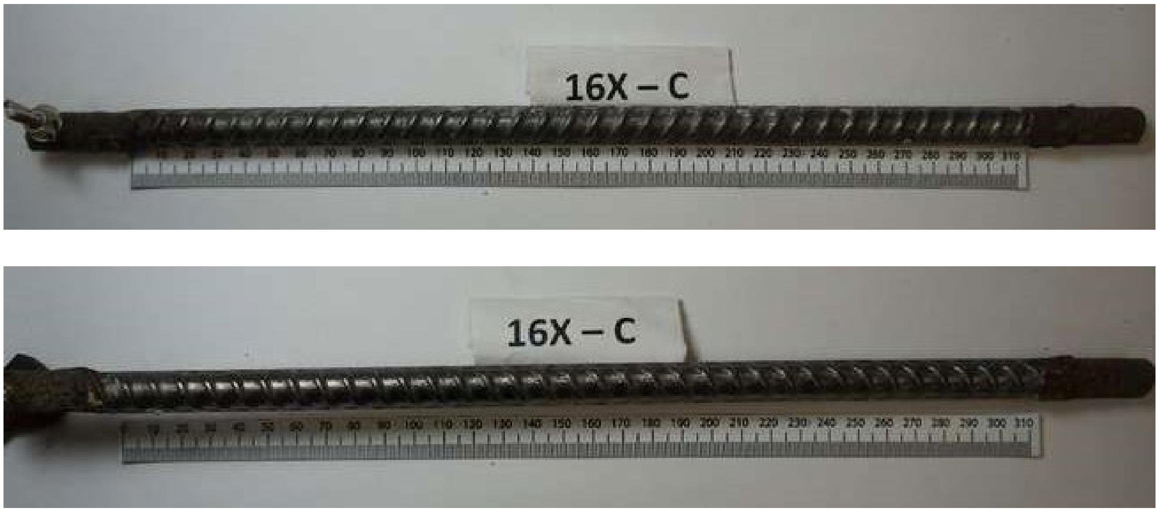

Figure 19. Sample 16X-C, side under the reservoir (first photo) and the opposite side of the reservoir (second photo) of the full rebar analyzed with the microscope after cleaning.

5.7. Corrosion Spots Evaluation from the Ultrasonic

Upon fully opening the sample and examining the areas where corrosion could be detected, a thorough and focused analysis was conducted using MATLAB. After opening the sample, the following analysis was performed for the positions in which the corrosive points were found with the help of the microscope and for the 60mm position, which also presented one of the most negative potentials. The Signed Concrete Cover represents the distance between the top of the concrete and the rebar and is often called the concrete cover. As previously stated, if concrete cover increases (smaller absolute value), this may imply that the concrete surface is deforming upward due to internal pressure or an internal crack. If this distance decreases (larger absolute value), on average, it can be attributed to a possible accumulation of corrosion products. Table X illustrates the signed concrete cover values for the 4 points mentioned, 20mm, 60mm, 110 mm, and 220 mm, in the four different time intervals in which the ultrasound test was performed.

Table X. Signed concrete cover for 20mm, 60mm, 110mm and 220mm vs. time.

Position [mm]	Date	Signed Concrete Cover (-d) [mm]
20	Jun-23	-25.85000
	Dec-23	-25.61840
	Feb-24	-25.59031
	May-24	-25.50685
60	Jun-23	-24.53319
	Dec-23	-25.62600
	Feb-24	-25.84823
	May-24	-26.02349
110	Jun-23	-27.01246
	Dec-23	-25.67701
	Feb-24	-25.62419
	May-24	-26.44327
220	Jun-23	-25.40357
	Dec-23	-25.44440
	Feb-24	-25.57170
	May-24	-24.80864

Table X shows that the 20mm position presented more positive values about the distance between the concrete and the rebar, with this difference being approximately 0.26 mm between June 2023 and May 2024. The position 60mm presented an increase in concrete cover distance over time of 1.5mm. The 110mm position presented a fluctuation over time going for more positive values until February 2024 and in May 2024 the concrete cover presented a decrease. Position 220mm increased around 0.17mm from June 2023 to February 2024, followed by a decrease almost 0.8mm from February 2024 to May 2024.

Chapter 5. Summary and Conclusions

Early experimentation and modeling showed an excellent match in amplitude and time-signature at the concrete surface between model and measurement, which indicated that the poro-elastic model uses a representative set of physical parameters. In the third and last year of this effort, sample 16X-C showed the most significant change when analyzing the potential from the moment the current application began until the end of the test. Following the forensic analysis, it was possible to identify localized and small corrosion points and not a uniform spread of corrosion throughout the rebar after opening the sample. A small but consistent rise in the distance between the concrete surface and the top of the rebar was noted at position 20 mm in Table X. This result is in alignment with the forensic analysis that confirmed the presence of brown rust at 20mm spot. This supports the rationale of employing the Ultrasonic method, along with the Biot-Stoll model, for analyzing the spread of corrosion over time.

References

- Abramowitz, M. and Stegun, I.A., “Handbook of Mathematical Functions,” New-York, Dover Publications (1970).
- An, Y. K., Jang, K., Kim, B., & Cho, S., “Deep learning-based concrete crack detection using hybrid images”, SPIE Sensors and Smart Structures Technologies for Civil, Mechanical, and Aerospace Systems 2018 (Vol. 10598, p. 1059812), 1-12, International Society for Optics and Photonics.
- Brogden M. Beaujean P.P., Presuel-Moreno F., Shaffer S., “Poro-Elastic Modeling of Corroding Reinforced Concrete using Biot-Stoll Model Inversion and High Frequency Ultrasonic”, Student Poster and Presentation, 2nd Annual TriDurLE Symposium, Honolulu, Hawaii, November 9-11, 2022.
- Beaujean P.P., Shaffer S., Presuel-Moreno F., Brogden M.. "Evaluation of the physical characteristics of reinforced concrete subject to corrosion using a poro-elastic acoustic model inversion technique applied to ultrasonic measurements." Journal of Infrastructure Preservation and Resilience 5, no. 1 (2024): 1-17.
- Beaujean P.P., Presuel-Moreno F., Brogden M., Ultrasonic Nondestructive Detection of Rebar Corrosion in Reinforced Concrete Using Biot-Stoll Model”, 2022 TriDurLE Seminar, Transportation Infrastructure Innovations for Durability and Resilience**,** Washington State University, February 16, 2022.
- Beaujean P.P., Presuel-Moreno F., Brogden M., “Ultrasonic Nondestructive Detection of Rebar Corrosion in Reinforced Concrete Using Biot-Stoll Model”, TriDurLE Symposium, Washington State University, December 6-7 (2021).
- Beaujean P.P., Joussein M., Schock S.G., “Influence of Depth-dependent Sediment Properties on the Pressure Reflection,” U.S. Navy Journal of Underwater Acoustics, Vol. 56, 85-111 (2006).
- Beaujean P.P., “Sediment Classification of the Sea Floor using the Chirp Sonar and the Biot Model”, MS Thesis, Florida Atlantic University, December 1995.
- Beebe, J.H. McDaniel S.T. and Rubano, L.A., " Shallow Water Transmission Loss Prediction Using the Biot Sediment Model," J. Acoust. Soc. Am. 71, 1417-1426 (1982).
- Berryman, J.G., "Long Wavelength Propagation in Composite Elastic Media," J. Acoust. Soc. Am. 68, 1809-1831 (1980).

- Biot M.A., “General Theory of Three-Dimensional Consolidation”, J.Appl.Phys. 12,155-164 (1941).
- Biot M.A., “Theory of Propagation of Elastic Waves in a Fluid-Saturated Porous Solid. I. Low-Frequency Range”, J.Acoust.Soc.Am. 28, 168-178 (1956).
- Biot M.A., “Theory of Propagation of Elastic Waves in a Fluid-Saturated Porous Solid. II. Higher Frequency Range”, J.Acoust.Soc.Am. 28, 179-191 (1956).
- Biot M.A., “Generalized Theory of Acoustic Propagation in Porous Dissipative Media”, J.Acoust.Soc.Am. 34, 1254-1264 (1962).
- Brogden M, “Estimation of the Physical Properties of Corroding Rebar in Reinforced Concrete using Biot-Stoll Model Inversion”, Master’s thesis, Florida Atlantic University, August 2022.
- Brogden M., Beaujean P.P., Presuel-Moreno F., “Ultrasonic Nondestructive Detection of Rebar Corrosion in Reinforced Concrete Using Biot-Stoll Model”, TriDurLE Symposium, Washington State University, December 6-7 (2021).
- Chaix J.F., Garnier V., Corneloup G., “Concrete Damage Evolution Analysis by Backscattered Ultrasonic Waves”, Elsevier NDT&E International 36 (2003), 461-469.
- Chang C.C., Yu C.P., Lin Y., “Distinction between Crack Echoes and Rebar Echoes based on Morlet Wavelet Transform of Impact Echo Signals”, Elsevier NDT&E International 108 (2019), 1-14: 102169.
- Da Silveira Pimental G., Small Anodic Polarization as a Mean to Modestly Accelerate Rebar Corrosion, Master’s thesis, Florida Atlantic University, August 2024.
- Fellinger, P., Marklein R., Langenberg K.J., and S. Klaholz. "Numerical modeling of elastic wave propagation and scattering with EFIT—elastodynamic finite integration technique." *Wave motion* 21, no. 1 (1995), 47-66.
- Hamilton, E.L., "Acoustic and Related Properties of the Sea Floor: Density and Porosity Profiles and Gradients," NUC Tech. Pap. #459, 1-47 (1975)
- Hovem, J.H. and Ingram, G.D., "Viscous Attenuation of Sound in Saturated Sand," J. Acoust. Soc. Am. 66, 1807-1812 (1979).
- Joussein M., Beaujean P.P., Schock S.G., “Influence of Depth-Dependent Sediment Properties on the Pressure Reflection Coefficient at Normal Incidence using the Biot-Stoll Model”, MTS/IEEE Oceans’04 Proceedings, pp. 1-11, Kobe, Japan, Sept. 2004.
- Laureti S., Ricci M., Mohamed M.N.I.B., Senni L., Davis L.A.J., Hutchins D.A., “Detection of Rebars in Concrete using Advanced Ultrasonic Pulse Compression Techniques”, Elsevier Ultrasonics 85 (2018), 31-38.
- Lin, C. C., Liu, P. L., Yeh, P. L., “Application of empirical mode decomposition in the impact-echo test”, NDT & E International, *42*(7) (2009), 589-598.
- Marshall R.M., “Acoustic Emission Associated with Embedded Metal Corrosion in a Concrete Slab”, Master’s Thesis, Florida Atlantic University, December 1982.
- Molero-Armenta M., Iturrarán-Viveros U., Aparicio S., Hernández, M. G., “Optimized OpenCL implementation of the elastodynamic finite integration technique for viscoelastic media”, Computer Physics Communications, 185(10) (2014), 2683-2696.
- Nakahata, K., Kawamura G., Yano T., Hirose S., "Three-dimensional numerical modeling of ultrasonic wave propagation in concrete and its experimental validation." Construction and Building Materials 78 (2015): 217-223.
- Plona, T.J., "Observation of a Second Bulk Compressional Wave in a Porous Medium at Ultrasonic Frequencies," Appl. Phys. Lett. 36, 259-261 (1980)

- Panametrics, Ultrasonic Transducers, Olympus, Technical Document, www.olympus-ims.com (2010).
- Philippidis T.P., Aggelis D.G., “Experimental Study of Wave Dispersion and Attenuation in Concrete”, Elsevier Ultrasonics 43 (2005), 584-595.

by

- Prassianakis I.N., Prassianakis N.I., “Ultrasonic Testing of Non-Metallic Materials: Concrete and Marble”, Elsevier Theoretical and Applied Fracture Mechanics 42 (2004), 191-198.
- Presuel-Moreno, F., "Corrosion Propagation of Carbon Steel Rebar with Different Concrete Covers and Concrete/Mortar Composition", in CORROSION 2015. NACE International, 2015.
- Presuel-Moreno F., Tang F., "Corrosion Propagation of Rebar Embedded in Low w/c Binary Concrete Blends Exposed to Seawater", in CORROSION 2018. NACE International, 2018.
- Shaffer S., “Optimized Parameters Fitting of a Poro-Elastic Acoustic Model with Ultrasonic Measurements for the Monitoring of Corroding Rebar in Reinforced Concrete”, Master’s thesis, Florida Atlantic University, August 2023.
- Stern M., Bedford A., Millwater H.R., “Wave Reflection from a Sediment Layer with Depth-Dependent Properties”, J.Acoust.Soc.Am. 77, 1781-1788 (1985).
- Stoll R.D., “Sediment Acoustics”, New York, Ed Springer-Verlag (1989).
- Stoll R.D., “Acoustic Waves in Ocean Sediments”, Geophysics 42, 715-725 (1977).
- Weng M.Y., “Detection of Deterioration of Reinforced Concrete by Acoustic Emission Techniques”, Master’s Thesis, Florida Atlantic University, December 1980.
- Xu, Y., Jin, R., “Measurement of reinforcement corrosion in concrete adopting ultrasonic tests and artificial neural network”, Construction and Building Materials, 177 (2018), pp.125-133.
- Xu, J., Wei, H., “Ultrasonic Testing Analysis of Concrete Structure Based on S Transform”, Hindawi Shock and Vibration (2019), 1-9: 2693141.
- Young J.D., “Acoustic Emissions Testing as a Nondestructive Monitor of Concrete Cracking due to Reinforcing Bar Corrosion”, Master’s Thesis, Florida Atlantic University, December 1982.